

Hypervelocity Candidates of G and K type: Classification of the Palladino et al. sample revised

Bachelor Arbeit aus der Physik
Vorgelegt von
Marco Volkert
17.09.2014

Dr. Karl Remeis-Sternwarte Bamberg
Friedrich-Alexander-Universität Erlangen-Nürnberg



Betreuer: Prof. Dr. Ulrich Heber & Dipl. Phys. Eva Ziegerer

Contents

1	Introduction	1
1.1	Hypervelocity Stars	1
1.2	Hertzsprung–Russell diagram	2
1.3	Structure of the Galaxy	3
1.4	Velocity	4
2	Parametrization of the Galaxy	7
2.1	Galactic Coordinate System	7
2.2	Potential models	7
2.3	Escape velocity	9
3	Results of Palladino et al.	11
3.1	SDSS	11
3.2	Selection Procedure	11
3.3	Potential Model	13
3.4	Doubts on these Results	13
3.4.1	Theoretical Predictions	13
3.4.2	Comparision of Proper Motions between Catalogs	14
4	Kinematic measurements	17
4.1	Radial velocity	17
4.1.1	Procedure	17
4.1.2	Results	18
4.2	Proper Motion	18
4.2.1	Photographic plates	18
4.2.2	Procedure	19
4.2.3	Results	20
5	Analysis of Orbits	23
5.1	Calculation of bound-probability	23
5.2	Interesting Candidates	24
5.2.1	Pal02	24
5.2.2	Pal12	26
5.2.3	Pal18	27
5.3	Kinematic properties	29
6	Conclusion and Outlook	33
A	Orbit Calculator Tables	35
B	Radial velocity fits of interesting stars	43
C	Proper motion fits of all stars	45

List of Figures	54
List of Tables	55
References	58
Acknowledgements	59
Erklärung	61

Abstract

Various mechanisms can accelerate stars to such high velocities that they are ejected out of the Galactic gravitational potential. Such stars are called Hypervelocity Stars (HVSs). HVSs are a puzzling feature of the Galactic halo. By means of reconstructing their trajectories the potential of the Galaxy can be deduced. Until now all but one confirmed HVSs are massive B-type stars, so it is an interesting aim to search for less massive stars, like G- and K-type with high velocities. Such a search was recently carried out by Palladino et al. (2014). They discovered 20 G- and K-type stars with space velocities of more than 600 km s^{-1} from the Sloan Digital Sky Survey (SDSS) and analysed their kinematics. The space velocity depends on the star's radial velocity, proper motion and distance. These stars have unusual high proper motions. Moreover the Palladino et al. (2014) stars are metal-poor and show α/Fe enrichment characteristic of population II stars. So it is very exciting to have a closer look on them. In this work these stars are revisited with own proper motion measurements and with the potential models of the Galaxy described by Irrgang et al. (2013). Reliable proper motions could be obtained for 14 of these stars. The kinematic analysis revealed that all but one are bound to the Galaxy and belong to the stellar population II. Only SDSSJ165956.02+392414.9 (Pal18) has a 25.55% probability of being unbound and has a quite unusual orbit. Better proper motion measurements are required to decide whether the star is a HVS or not.

Chapter 1

Introduction

1.1 Hypervelocity Stars

Numerical simulations by Hills (1988) showed that a supermassive black hole (SMBH) can accelerate stars to very high velocities by the tidal disruption of a binary system. One component is captured, whereas the angular momentum is transferred to the other one. Genzel et al. (2003) and Schödel et al. (2003) discovered a SMBH in the center of the Galaxy (GC). The theoretical estimations on the ejection rate by the SMBH ($\sim 4 \cdot 10^{-6} M_{\odot}$) are up to $\sim 10^{-4} \text{yr}^{-1}$ (Yu & Tremaine (2003)), which is 100 times larger than for any expected other mechanism.

Hence stars were predicted to reach velocities so high that they are no longer bound to the Galaxy. Brown et al. (2005) discovered the first Hypervelocity star (HVS) (SDSS J090745.0+024507). The Galactic rest-frame velocity v_{GRF} was determined to be 709 km s^{-1} . As it is a main sequence star of $3M_{\odot}$, it is about 110 kpc away. It was named HVS1 and nearly all HVS discovered later were named continuously. Shortly thereafter two more HVS were discovered by Hirsch et al. (2005) (HVS2) and Edelmann et al. (2005) (HVS3).

Apart from the ejection mechanism by a SMBH other mechanisms have been suggested until now, like the ejection by a binary black hole, the ejection by a Supernova in a binary system and some more. Stars ejected from the Galactic disk are called runaway stars. Heber et al. (2008) discovered the first unbound example of them. Sometimes the different nomenclature of HVS leads to some confusion: Often (e.g. Kenyon et al. (2014)) only stars ejected by the SMBH are referred to as HVSs. But while searching for stars with high Galactic rest frame velocities v_{GRF} , you preliminary do not know where the star comes from, so in this work the term HVS will be used for stars with high v_{GRF} .

To test the above described different scenarios, surveys for HVSs have to be performed. At the beginning of 2014 the discoverers of the first HVS, Brown et al. (2014), published their completed spectroscopic survey for unbound HVS. At least 16 unbound stars were found with the Multiple Mirror Telescope (MMT) during the survey. Accordingly 21 unbound HVS have been discovered so far.

Brown et al. (2014) searched only for stars with colors of $2.5 - 4M_{\odot}$ stars, because these should not exist in the outer regions of the galactic halo (50 kpc – 120 kpc) if they weren't ejected there. The radial motions of the survey stars are higher than the escape velocity, hence no proper motion was needed to prove the stars to be HVSs. Furthermore they were confirmed to be main sequence B stars at 50 – 120 kpc distances.

An extrapolation (Brown et al., 2014) shows that there should be ~ 300 unbound HVSs of masses $2.5 - 4M_{\odot}$ over the entire sky within $R < 100 \text{ kpc}$, so the ejection rate of those HVS would be $1.5 \cdot 10^{-6} \text{ yr}^{-1}$.

Taking the Salpeter initial mass function (IMF), the total rate should be about $2.5 \cdot 10^{-4} \text{ yr}^{-1}$ quite similar to the theory of Hills (1988). Brown et al. (2014) concludes that the flight-time distribution is best described by continuous ejection (as expected for Hills’ scenario), but some ambiguity still remains. For example, Brown et al. (2014) found that half of the discovered HVSs form a clump in the constellation Leo, where a satellite galaxy is located. Surveys on the southern hemisphere should bring better understanding, if all HVSs are either ejected continuously or during events, like the approach of a binary black hole or the tidal disruption of a satellite galaxy. Later ones would form spacial distributions looking like rings and clumps.

But even looking at lower mass stars could bring new insight in HVS origins. Such a search for low mass HVS candidates was reported by different authors. Li et al. (2012) reported 13 metal poor F-type HVS candidates in SDSS. But they note that all but one could be bound halo stars, depending on the galactic potential applied. Zhong et al. (2014) published 28 HVS candidates of spectral types A to K in the near solar neighbourhood (in a distance of less then 3 kpc) in the first data release of Large Sky Area Multi-Object Fibre Spectroscopic Telescope (LAMOST). Those stars are claimed to own a GRF velocity of more than 300 kms^{-1} , 12 of them are suggested to be most likely HVSs. Moreover they claim that their spectra of the stars are very reliable and show no sign of binarity. They even compared the obtained proper motions with PPMXL and UCAC4 and didn’t find any significant difference. Palladino et al. (2014) found 20 G and K type HVS candidates in the SDSS data base with high probabilities of being unbound. Their sample is characterised by low metallicity and abnormal high proper motions. Therefore a detailed study seems worthwhile.

1.2 Hertzsprung–Russell diagram

How stars of different masses behave and evolve can be best described with the help of the Hertzsprung–Russell diagram (HRD). Therein the luminosity L of the star, which is proportional to the absolute magnitude M_v , is plotted against the effective temperature T_{eff} . By the end of the 19th century astronomers began to categorise stars in different spectral type, which was later on shown to correspond to T_{eff} . B - stars are very hot, massive and bright, whereas G - stars are a bit like our sun. During a star’s main lifetime nuclear fusion of hydrogen to helium takes place. Stars in this stage follow the so-called main sequence (MS). So by knowing the spectral type of the star the position in the HRD can be deduced and therefore the absolute magnitude M_v can be calculated. As described later this is necessary to determine the distance of the star to our solar system. Furthermore there is a relation between luminosity and mass of a star on the MS (Voigt (2012)) from which the stellar lifetime τ_{MS} can be deduced:

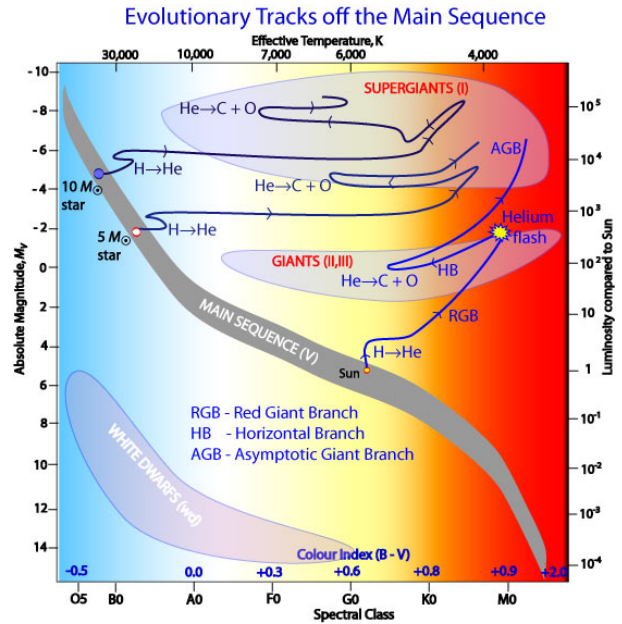


Figure 1.1: **HRD**: plot of effective temperature against luminosity, **main sequence**: stars burning hydrogen own a relation between temperature and luminosity¹

¹http://outreach.atnf.csiro.au/education/senior/astrophysics/stellarevolution_postmain.html

- low mass ($M < 0.8M_{\odot}$) :

$$L \sim M^{2.8} \rightarrow \tau_{MS} \sim 10^{10} \left(\frac{M_{\odot}}{M} \right)^{1.8} \quad (1.1)$$

- high mass ($M \geq 0.8M_{\odot}$):

$$L \sim M^4 \rightarrow \tau_{MS} \sim 10^{10} \left(\frac{M_{\odot}}{M} \right)^3 \quad (1.2)$$

The stellar lifetime is directly proportional to the "fuel" a star can burn and inversely proportional to the energy a star loses $\Rightarrow \tau_{MS} \sim \frac{M}{L}$. So the bigger a star is, the shorter it lives. This work mainly discusses stars of about $1M_{\odot}$ or lower mass, which live more than 10 Gyr.

When the hydrogen in the core of the star is exhausted, the core contracts and the envelope of the star is inflated by the released energy to become a red giant. During the core's contraction the density and temperature in the core rises until fusion of Helium can start. For low mass stars, the electron gas is degenerated leading to the so-called "Helium flash". After that the star is located on the "horizontal branch" (HB) in the HRD and Helium fusion takes place in the core. When Helium is exhausted the further destiny of the star depends on its mass. Low mass stars undergo the AGB stage, where H and He are fused in two shells whereby the core is contracting. In this stage the star losses its envelope during stellar winds and a degenerated Helium core is left over, the so-called white dwarf. Whereas high mass stars will fuse higher elements and end up in a supernova.

1.3 Structure of the Galaxy

Our Galaxy can basically be divided in three components (see figure 1.2):

- **Bulge:** In the central part of the Galaxy there is an ellipsoidal accumulation of mainly old metal rich stars.
- **Disk:** The disk is a flat region containing gas clouds where new stars can form. They are called Population I stars. The differential rotation of the disk leads to the formation of density waves, the so-called spiral arms. Models for the Galactic gravitational potential ignore those spiral arms, because it is too difficult to parametrize them. Moreover the disk can be subdivided in thin and thick disk. The latter one is vaster and not as flat as the thin disk.
- **Halo:** The **stellar halo** of the Galaxy consists of globular clusters of metal poor, very old stars and some isolated metal poor stars. These stars are called Population II. In contrast to the disk, the halo does not rotate. So the stellar halo is characterized by an equal number of stars moving in

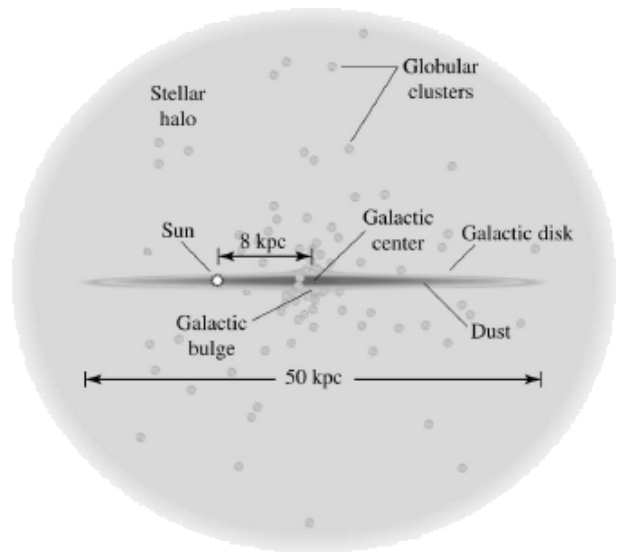


Figure 1.2: Structure of the Milky Way²: Bulge, Disk, Halo

²lecture Astronomy II: slide 20-12

and against the direction of Galactic rotation. Furthermore radial velocity curves of the galaxy showed that most of the galaxy mass is invisible and presumably spherically distributed around the galaxy - the **dark matter halo**.

The metallicity of stars is defined as the ratio of the number of iron atoms to the number of hydrogen atoms with respect to the sun:

$$[\text{Fe}/\text{H}] = \log(\text{Fe}/\text{H})_* - \log(\text{Fe}/\text{H})_{\odot} \quad (1.3)$$

With the help of metallicity a statement about the conditions at the birth of a star can be made. In regions with high star forming rate a lot supernova exploded and so the gas was enriched with iron and other heavier elements. Thus the the metallicity can be an indicator for birth place of a star. Pauli et al. (2006) divided a sample of G and F type main sequence stars into thin disk, thick disk and halo stars with the help of metallicity:

- thin disk: $-0.3 < [\text{Fe}/\text{H}]$ and $[\text{Mg}/\text{Fe}] \leq 0.2$
- thick disk: $-1.05 \leq [\text{Fe}/\text{H}] \leq -0.3$ and $0.3 \leq [\text{Mg}/\text{Fe}]$
- halo: $[\text{Fe}/\text{H}] < -1.05$

Whereby Mg is a so-called α -element, which means that it resulted from α -particle (helium atomic nucleus) capture process during fusion in a star. As it can be seen by this classification, stars belonging to the thick disk show α -enrichment.

In this way they calibrated the velocity based classification of membership to galaxy parts of their sample of white dwarfs (see Sect. 5.3).

1.4 Velocity

The full 3D velocity of a star is composed of a radial and two transversal components measured in relation to the sun. The radial one is parallel to our line of sight. Due to the Doppler effect the wavelength is shifted. By analysing spectral lines this component can be measured quite well. In contrast to the previous one the transversal velocity is perpendicular to the line of sight and has no influence on the spectrum. In order to measure this component, the angular motion on the sky, named proper motion μ in radian/s, and the distance d to the star have to be determined: $v_t = \mu \cdot d [1 \frac{mas}{yr} \cdot kpc = 4.612 \frac{km}{s}]$

Both are quite difficult tasks. For the calculation of distance one has to know how bright a star would be if it were in a distance of 10pc. This is called the absolute magnitude M_v . M_v can be acquired by knowing the evolutionary state of the star and by comparing this with the HRD. Then the distance

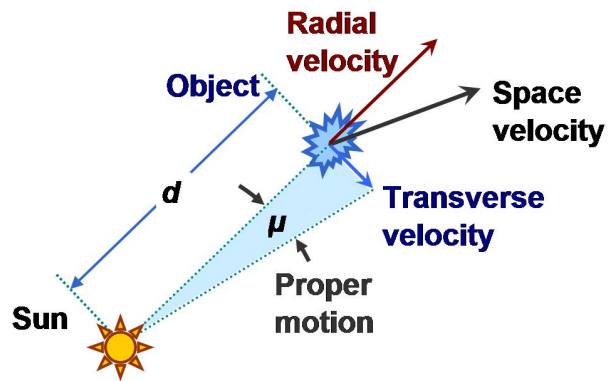


Figure 1.3: Velocity components³:

radial velocity: Doppler shift,

transverse velocity: composed out of the proper motion μ (angular motion on the sky) and the distance d of the star

³http://upload.wikimedia.org/wikipedia/commons/f/f2/Proper_motion.JPG

can be calculated by measuring the apparent magnitude m_v :

$$d = 10^{\frac{m_v - M_v}{5} - 1} \quad (1.4)$$

Yet for determination of proper motion, the comparison of the position of the star on different time epochs is needed. The complete proper motion is constituted by an component in right ascension and one in declination:

$$\mu^2 = \mu_\alpha^2 \cdot \cos(\delta)^2 + \mu_\delta^2.$$

The consequence of above considerations is that the farther away a star is, the more difficult it is to measure its space velocity.

Chapter 2

Parametrization of the Galaxy

2.1 Galactic Coordinate System

For a better understanding of the kinematic behaviour of stars, the position and velocity have to be set into relation to our Galaxy. Therefore a Galactic Cartesian system (X, Y, Z) is used. The origin of this system is in the Galactic centre (GC), the x-axis points from the sun to the GC, the y-axis points in the direction of Galactic rotation and the z-axis points to the North Galactic Pole. In this system the sun's coordinates are: $(X, Y, Z)_{\odot} = (-8.33, 0, 0)$ ¹ The velocity in this system is defined as:

$$\vec{v} = \frac{d}{dt} \begin{pmatrix} X \\ Y \\ Z \end{pmatrix} = \begin{pmatrix} v_x \\ v_y \\ v_z \end{pmatrix} \quad (2.1)$$

But often cylindrical Coordinates V, U, Z are used for the velocity. The Local Standard of Rest (LSR) is a reference frame located at the position of the sun. Its time evolution equals the stars' average movement in the solar neighbourhood: $(V, U, W)_{LSR} = (11.1, 12.24, 7.25)$ ². Therefore the velocity of the sun is $(V, U, W)_{\odot} = (11.11, 232.24, 7.25)$.

2.2 Galactic gravitational potential models

As described by Irrgang et al. (2013) three potential models of the Galaxy were used. All models are of the same structure:

$$\Phi(r, z) = \Phi_{\text{bulge}}(R(r, z)) + \Phi_{\text{disk}}(r, z) + \Phi_{\text{halo}}(R(r, z)) \quad (2.2)$$

in which (r, Φ, z) are cylindrical coordinates and $R(r, z) = \sqrt{r^2 + z^2}$ is the spherical radius.

$$\Phi_{\text{bulge}} = -\frac{M_b}{\sqrt{R^2 + b_b^2}} \quad (2.3)$$

¹Irrgang et al. (2013)

²Schönrich et al. (2010)

$$\Phi_{\text{disk}} = -\frac{M_d}{\sqrt{r^2 + (a_d + \sqrt{z^2 + b_d^2})^2}} \quad (2.4)$$

in which M_i are weighting factors of the components and a_i, b_i are scale lengths. ($i = b, d, h$). For the bulge and the disk component the weighting factors equal the component's masses. Only the halo component is varied in the different models, whereby it should be mentioned that even the parameters of the disk and the bulge differ:

Model I

Model I is an updated version of Allen & Santillan (1991). It was designed to be as simple as possible and mathematically analytic. Λ is a cut-off parameter introduced to prevent a infinite large halo mass, which would be unphysical. Furthermore the parameter γ is a priori indeterminate, so by setting $\gamma = 2$ no restriction is made.

$$\Phi_{\text{halo}}(R(r, z)) = \begin{cases} \frac{M_h}{a_h} \left(\frac{1}{(\gamma-1)} \left(\frac{1 + \left(\frac{R}{a_h}\right)^{\gamma-1}}{1 + \left(\frac{\Lambda}{a_h}\right)^{\gamma-1}} \right) - \frac{\left(\frac{\Lambda}{a_h}\right)^{\gamma-1}}{1 + \left(\frac{\Lambda}{a_h}\right)^{\gamma-1}} \right) & \text{if } R < \Lambda \\ -\frac{M_h}{R} \frac{\left(\frac{\Lambda}{a_h}\right)^{\gamma}}{1 + \left(\frac{\Lambda}{a_h}\right)^{\gamma-1}} & \text{otherwise} \end{cases} \quad (2.5)$$

Model II

This truncated, flat rotation curve model was first presented by Wilkinson & Evans (1999) and calibrated through satellite galaxies and globular clusters.

$$\Phi_{\text{halo}}(R) = -\frac{M_h}{a_h} \cdot \ln \left(\frac{\sqrt{R^2 + a_h^2} + a_h}{R} \right) \quad (2.6)$$

Model III

Model III was suggested by Navarro et al. (1997) with the help of cosmological simulations. In contrast to the first ones, it is the only one with an scientific justification and not only a mathematical one.

$$\Phi_{\text{halo}}(R) = -\frac{M_h}{R} \cdot \ln \left(1 + \frac{R}{a_h} \right) \quad (2.7)$$

Irrgang et al. (2013) reinvestigated those potentials by using various observational constraints, including rotation curve of the galaxy, measured by terminal velocities and maser, mass and surface densities and the velocity dispersion in Bade's window. The most prominent constraint was the peculiar star SDSSJ153935.67+023909.8 to be bound. This is a blue horizontal branch halo star with a Galactic rest frame velocity of about 694_{-221}^{+300} km s⁻¹ approaching the Galactic disk. If the star was unbound, i.e. the star would only have a single encounter with the Galactic disk without coming back, this would indicate either an extragalactic origin or an extreme dynamical event with a globular cluster or a satellite galaxy. The assumption that the star is bound is therefore justified by the unlikelihood of these scenarios.

All models can reproduce the observations equally well. Though this might seem strange, this is due to too less observational constraints.

By fitting the above described constraints, Irrgang et al. (2013) obtained following values (For errors and more values see Irrgang et al. (2013)):

Table 2.1: Parameters obtained by Irrgang et al. (2013) for different potential models

parameter	Model I	Model II	Model III
r_{\odot}	8.40	8.35	8.33
M_h	1018	69725	142200
a_h	2.56	200	45.02
$M_{R < 200\text{kpc}} (10^{12} M_{\odot})$	1.9	1.2	3.0

2.3 Escape velocity

HVSs were originally defined as stars which are unbound to the galaxy. This means that the star exceeds the local escape velocity at the star's position in the galaxy and will never come back. The local escape velocity v_{esc} is defined as the velocity for which the kinetic energy E_{kin} equals the potential energy E_{pot} :

$$E_{\text{kin}} = E_{\text{pot}} \Leftrightarrow \frac{1}{2} \cdot v_{\text{esc}}^2 = \Phi_{\text{local}} \Leftrightarrow v_{\text{esc}} = \sqrt{2 \cdot \Phi_{\text{local}}} \quad (2.8)$$

Here $\Phi_{\text{local}} = \frac{E_{\text{pot}}}{m}$ denotes the galactic potential at the stars position and m the star's mass, respectively. The "orbit calculator" programme designed by Irrgang et al. (2013) calculates the total energy $E'_{\text{total}} = E'_{\text{kin}} - E'_{\text{pot}}$ of a star in units of $\frac{\text{kpc}^2}{\text{Myr}^2}$, so it is quite easy to decide whether a star is bound ($E'_{\text{total}} < 0$) or not ($E'_{\text{total}} > 0$). At this point it should be mentioned that the escape velocity and therefore even the bound-probability varies between different potential models that are used.

Chapter 3

Results of Palladino et al.

3.1 SDSS

Most of the HVSs have been discovered using the database of the Sloan Digital Sky Survey (SDSS)³, the largest automatic photometric and spectroscopic sky survey ever (Brown et al. (2014)). The 2.5m telescope, used for SDSS, at Apache Point Observatory in the southeast of New Mexico covers major parts of the northern hemisphere. Five filters are utilized (u', g', r', i', z').

Nearly annually new data releases (DR) are published via the Internet, this bachelor thesis uses DR10. The DR provide a huge data base in which nearly all interesting properties of the stars, like radial velocity, proper motion and so on, are listed and can be accessed via SQL statements. These data are calculated via automatic algorithms. So errors may occur. The bigger the sample is, the more probable it is that some values are a statistical illusion. For the stars, analysed in this Bachelor thesis, no difference in the data of DR9 compared to DR10 was noticed.

3.2 Selection Procedure

Although the ejection mechanism for HVSs of low mass as for high mass should be quite similar, no G and K type HVS have been found yet. This significant lack would indicate that the initial mass function at the GC is quite top-heavy or the mechanism is more complex than previously thought.

So Palladino et al. (2014) thoroughly scrutinized SEGUE (Sloan Extension for Galactic Understanding and Exploration) from SDSS DR9 for G and K dwarf stars. SEGUE took medium resolution spectra ($R \approx 1800$) over a broad spectral range ($3800 - 9200\text{\AA}$) of ≈ 240.000 stars of different spectral types. Palladino et al. (2014) selected their targets by using a simple color magnitude selection criteria:

- G dwarfs: $14.0 < r < 20.2$ and $0.48 < (g - r) < 0.55$
- K dwarfs: $14.5 < r < 19.0$ and $0.55 < (g - r) < 0.75$

Colour and magnitude were corrected for interstellar dust extinction. The spectral analysis was carried out by DR9 SEGUE Stellar Parameter Pipeline (SSPP). According to the gravities derived, all the stars are actually dwarf stars.

³<http://www.sdss.org/>

To estimate whether they are HVSs the radial velocity and proper motion, also obtained by SDSS, were translated to Galactic Cartesian coordinates and a total velocity threshold of 600 km s^{-1} was applied. The kinematic analysis heavily relies on the stars' proper motions.

To check if SDSS proper motions are reliable, a number of criteria defined by Munn et al. (2004) were applied. It was concluded that 3 stars have a probability of less than 0.5% (named "clean") and 17 stars of less than 1.5% (named "reliable") to be contaminated.

In spite of these findings the ratio of transversal to radial velocity was larger than expected for a normal distribution of stars (see Figure 3.1). A normal distribution would have a ratio of $\sqrt{2}$ indicated by the red line, whereas most of these stars show a ratio of larger than 5 indicated by the blue line.

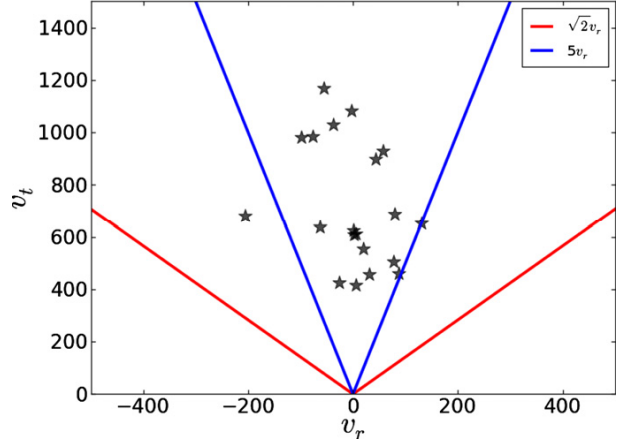


Figure 3.1: ratio of transversal to radial velocity: A normal distribution of stars is described by a $\sqrt{2}$ times higher v_t than v_r as displayed by the red line (Palladino et al., 2014, Figure 1). This sample has obviously abnormal high v_t

Table 3.1: Stars of Palladino:

metallicity, distance to the star d , radial velocity v_r , tangential velocity v_t , Galactic rest frame velocity v_{GRF} , minimal velocity v_{min} , escape velocity v_{esc} and bound-probability are listed

Pal	IAU-Name	[Fe/H]	[α /Fe]	d (kpc)	v_r	v_t	v_{GRF}	v_{min}	v_{esc}	% Bound
1	J060306.77+825829.1	-0.06	0.10	3.70	-76.0	56.1	802.2	92.2	533.6	6.35
2	J023433.42+262327.5	-0.15	0.09	5.68	-25.6	15.7	628.6	290.0	517.3	7.43
3	J160620.65+042451.5	-0.91	0.40	4.06	31.7	23.7	641.8	195.1	588.9	34.88
4	J113102.87+665751.1	-0.83	0.46	1.04	-54.9	237.7	1296.7	587.4	552.3	0.0
5	J185018.09+191236.1	-0.34	0.19	3.19	58.0	61.5	1086.8	378.9	576.5	0.04
6	J035429.27-061354.1	-0.55	0.26	3.13	80.2	46.2	916.3	286.6	534.5	0.07
7	J064337.13+291410.0	-0.55	0.35	3.06	20.4	38.1	793.9	285.0	530.2	0.30
8	J202446.41+121813.4	-0.65	0.26	2.48	6.26	51.8	769.1	376.3	570.3	1.01
9	J011933.45+384913.0	-0.67	0.22	3.31	-36.9	65.5	937.3	185.2	536.3	1.20
10	J172630.60+075544.0	-0.67	0.39	3.82	-2.2	59.7	992.9	233.5	591.0	1.34
11	J073542.35+164941.4	-0.23	0.12	3.70	78.2	28.8	712.9	285.4	527.3	2.89
12	J025450.18+333158.4	-0.70	0.16	3.14	-62.4	42.8	731.4	265.1	532.9	3.77
13	J134427.80+282502.7	-1.27	0.44	2.91	2.5	44.0	715.7	270.5	557.0	4.42
14	J225912.13+074356.5	-0.56	0.37	4.60	-97.8	44.9	840.7	121.8	550.0	5.86
15	J095816.39+005224.4	-0.80	0.28	2.22	1.6	59.2	649.8	248.7	546.5	15.98
16	J074728.84+185520.4	-0.24	0.13	3.26	43.9	58.1	672.8	55.3	530.7	19.70
17	J064257.02+371604.2	-0.33	0.21	1.78	6.2	49.1	601.4	305.4	540.9	20.01
18	J165956.02+392414.9	-1.14	0.48	4.35	-205.1	33.0	649.1	170.0	562.3	21.30
19	J110815.19-155210.3	-0.99	0.35	4.56	131.2	30.1	622.7	162.0	545.8	23.69
20	J145132.12+003258.0	-0.59	0.12	5.88	88.0	16.5	606.7	193.1	579.8	43.24

Kinematic parameters obtained by Palladino et al. (2014) and the stars' metallicities are listed in Table 3.1. Apparently the low [Fe/H] and high α -enrichment are more consistent with population II star, whereby an origin in the galactic disk cannot be excluded. The bound probability was obtained by Monte Carlo simulations of possible orbits.

In the following rest these candidates will be referred to as Pal01,...,Pal20 to avoid confusion with Brown et al. (2005), unlike Palladino et al. (2014).

3.3 Potential Model

For orbit calculation, Palladino et al. (2014) used a Galactic potential model consisting of:

- a spherical Hernquist bulge (Hernquist, 1990)
- a Miyamoto-Nagai disk (Miyamoto & Nagai, 1975)
- a Navarro - Frenk - White dark matter halo (Navarro et al., 1997)

As the bulge and disk component will not effect the escape velocity of these stars significantly, it is mainly interesting to compare NFW-Parameters of Irrgang et al. (2013) with Palladino et al. (2014). But first the formalism of different authors have to be compared: (Navarro et al., 1997; Łokas & Mamon, 2001)

In the original paper of Navarro et al. (1997) the following density stratification of the Galactic halo is used:

$$\frac{\rho(r)}{\rho_c^0} = \frac{\delta_{char}}{\left(\frac{r}{r_s}\right) \left(1 + \frac{r}{r_s}\right)} = \frac{\delta \cdot r_s^3}{r(r_s + r)^2} \quad (3.1)$$

Whereas Irrgang et al. (2013) uses:

$$\rho(R) = \frac{M_h}{4\pi} \frac{1}{(a_h + R)^2 R} \quad (3.2)$$

$$\rightarrow r_s = \frac{R_{vir}}{c} = a_h \quad (3.3)$$

with $R_{vir} = 200$ kpc and $c = 10$ as applied by Palladino et al. (2014) results in:

	a_h in kpc	M_h in M_{solar}
Palladino et al.	20	10^{12}
Irrgang et al.	45	$3 \cdot 10^{12}$

Thus the NFW model from Irrgang et al. (2013) used in this Bachelor thesis is quite more massive. Hence stars need a higher velocity to escape the potential.

Finally it should be mentioned that Palladino et al. (2014) excluded the origin in the central region of the Galaxy and an origin in M31 for the whole sample.

3.4 Doubts on these Results

3.4.1 Theoretical Predictions

Kenyon et al. (2014) investigated analytically and numerically the behaviour of HVSs and runaway stars in a model of the Galaxy. The possible velocities were calculated via models for (i) the ejection through the SMBH, (ii) a supernova in a binary system and (iii) a multi-body interaction in a globular cluster. Then distributions and properties of simulated HVSs and runaway stars were evaluated and compared to observations.

The HVS sample discovered by Brown et al. (2014) matches the theoretical estimations for distant HVSs very well and the possibility for stars of this sample to be runaway stars could be widely excluded. Whereas the sample of Palladino et al. (2014) does not match the theoretical estimations at all.

The lines in figure 3.2 represent contours of constant stellar density of simulated stars. Of all simulated stars an amount of 50% are located within the inner contours and 90% are located within the outer ones. The green colour results from a simulation of runaway stars, the purple one from predictions for HVSs and the black dots are the sample of Palladino et al. (2014). Obviously all but three of this sample are far beyond the contours.

Kenyon et al. (2014) note that either the proper motions used by Palladino et al. (2014) are incorrect or their model has to be modified considerably.

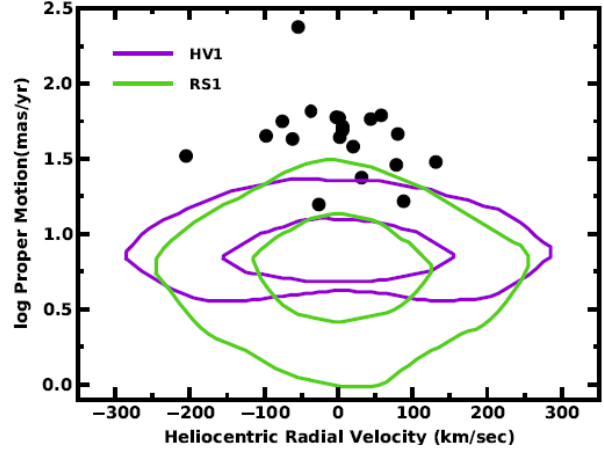


Figure 3.2: Doubts on Palladino et al. (2014) by a theoretical model (Kenyon et al., 2014, Figure 25), **purple:** HVSs, **green:** runaway stars, **inner contours:** 50% of all simulated stars, **outer contours:** 90% of all simulated stars, **black dots:** sample of Palladino et al. (2014)

3.4.2 Comparison of Proper Motions between Catalogs

The first check if the proper motions from SDSS are reliable, was to compare the used proper motions within different astronomic catalogs. In the following a short overview of the used catalogs are given:

- **The USNO-B1.0 Catalog (Monet et al., 2003)** contains positions, proper motions and magnitudes in different passbands. The data were taken from the Schmidt plates described in Sec. 4.2.1.
- **The Naval Observatory Merged Astrometric Dataset (NOMAD) (Zacharias et al., 2004)** takes the "best" values of the Hipparcos, Tycho-2, UCAC2, USNO-B1.0 and 2MASS catalog. For the stars discussed here, the proper motions of NOMAD are identical to the USNO-B1.0 catalog, so it seems that only data of USNO-B1.0 were available for these stars.
- **The PPMXL Catalog (Roeser et al., 2010)** combines data of the USNO-B1.0 Catalog with data from 2MASS to obtained recalculated positions and proper motions.
- **The fourth U.S. Naval Observatory CCD Astrograph Catalog (UCAC4) (Zacharias et al., 2012)** The proper motions were obtained by comparing different catalogs with significant difference in epoch. Moreover this catalog only covers stars down to a magnitude of 16 and no Schmidt plate data were used. So only Pal04 is contained in this catalog.
- **The Initial Gaia Source List (IGSL) (Smart & Nicastro, 2014)** uses the Tycho2, LQRF, UCAC4, SDSS-DR9, PPMXL, GSC23, GEPC, OGLE, Sky2000 and 2MASS catalogs to obtain a collection for the treatment of the first data which Gaia will deliver.

In tables 3.2 and 3.2 the proper motions from the different catalogs are listed. Sometimes there are two entries in a catalog for the same star. As one can see the PPMXL, USNO, NOMAD and Gaia catalog are

quite similar, whereas there are some differences to SDSS. Moreover it is remarkable that the UCAC4 proper motion data for Pal04 are significantly lower than in all other catalogs (Initial Gaia uses the UCAC4 result).

Since some discrepancies were found among the different catalogs, it seemed to be worthwhile to perform independent proper motion measurements.

Table 3.2: Comparison of proper motion components between different catalogs

$$\mu_{\alpha} \cdot \cos(\delta)$$

Pal	SDSS	PPMXL	USNO	Nomad	initial Gaia	UCAC4	Gaia alternative	PPMXL alternative
1	38.3 ± 2.6	39.9	36	36	39.9			
2	-2.6 ± 3.0	1.1	0	0	1.1			
3	23.6 ± 3.0	10.2	0	0	10.2			
4	-117.2 ± 5.9	-126.5	-122	-122	-17.5	-17.5		
5	-0.5 ± 3.1	-3.0	-2	-2	-3.0			
6	-41.6 ± 5.5	-54.4	-60	-60	-54.4			
7	-23.6 ± 2.6	-24.4	-22	-22	-24.4			3.0
8	-18.9 ± 2.9	-12.3	-16	-16	-12.3			
9	4.8 ± 2.9	6.2	8	8	6.2			
10	19.7 ± 2.9	19.2	20	20	19.2			
11	7.6 ± 2.8	12.4	10	10	12.4			
12	19.4 ± 2.8	13.2	6	6	13.2			
13	39.6 ± 3.0	30.2	38	38	30.2			
14	-5.7 ± 3.9	-6.1	-6	-6	-0.4		-6.1	
15	-58.6 ± 5.4	-63.5	-58	-58	-63.5			
16	0.8 ± 5.7	-2.9	0	0	-2.9		-3.1	-3.1
17	25.2 ± 2.5	21.4	16	16	21.4			
18	7.2 ± 3.1	8.0	10	10	8.0			
19	-28.8 ± 6.9	-37.2	-30	-30	-37.2			
20	15.4 ± 5.8	25.1	32	32	25.1			

$$\mu_{\delta}$$

Pal	SDSS	PPMXL	USNO	Nomad	initial Gaia	UCAC4	Gaia alternative	PPMXL alternative
1	-41 ± 2.6	-38.0	-36	-36	-38.0			
2	15.5 ± 3.0	2.4	0	0	2.4			
3	-1.6 ± 3.0	-2.3	0	0	-2.3			
4	206.8 ± 5.9	213.4	218	218	-19.5	-19.5		
5	61.5 ± 3.1	66.1	70	70	66.1			
6	20.1 ± 5.5	38.0	32	32	38.0			
7	29.9 ± 2.6	27.7	28	28	27.7			-8.5
8	48.3 ± 2.9	41.5	50	50	41.5			
9	-65.3 ± 2.9	-61.8	-58	-58	-61.8			
10	-56.4 ± 2.9	-52.5	-50	-50	-52.5			
11	27.7 ± 2.8	18.5	18	18	18.5			
12	38.1 ± 2.8	24.1	24	24	24.1			
13	-19.1 ± 3	-16.0	-10	-10	-16.0			
14	-44.5 ± 3.9	-54.2	-52	-52	3.4		-54.2	
15	8.1 ± 5.4	7.0	10	10	7.0			
16	-58.1 ± 5.7	10.6			10.6		-52.6	-52.6
17	42.1 ± 2.5	38.7	36	36	38.7			
18	-32.2 ± 3.1	-25.6	-24	-24	-25.6			
19	8.7 ± 6.9	2.2	12	12	2.2			
20	-5.8 ± 5.8	-6.1	-8	-8	-6.1			

Chapter 4

Kinematic measurements

4.1 Radial velocity

4.1.1 Procedure

The radial velocity of stars can be measured via the Doppler shift of spectral lines. Therefore spectra were obtained from the SDSS data base. SDSS took some individual spectra for every star, studied in this work, and averaged them to increase the signal to noise ratio (S/N). The S/N strongly correlates with the apparent magnitude of the star, as SDSS uses nearly the same exposure time for every star. As mentioned before the stellar parameters, i.e. effective temperature T_{eff} , surface gravity $\log g$, angular velocity $v \sin i$ and radial velocity v_{rad} , were already calculated by SSPP. In this work only a consistency check was performed.

First we estimated the stellar parameters with the help of Atlas 9⁴ model grids and the colours obtained by SDSS. Furthermore prominent solar absorption lines were chosen, as the analysed stars are of G and K type. Then the FITSB2-Routine of Napiwotzki et al. (2004) in combination with atmospheric grids of Munari et al. (2005) were used to obtain the radial velocity. This routine compares synthetic spectra calculated from model atmospheres with the data and minimises χ^2 via a simplex algorithm. Beginning with some starting values the algorithm successively searches for better fitting parameters until a (local) χ^2 minimum is reached. Moreover it can be selected whether all parameters or only designated ones are fitted. Once all parameters were fitted and once only the radial velocity. Secondly the stellar parameters of SSPP were taken and only the radial velocity was fitted. Once with zero as the starting value and once with the v_{rad} of SSPP as the starting value. This was done to ensure that the fit was not in a local minimum of χ^2 , but in a global one.

Finally v_{rad} was fitted to the individual spectra applying the best stellar parameters obtained before by using the averaged spectra. In this way radial velocity variations can be searched for, which may indicate that the star may be a binary.

Two main problems were present in nearly all fits: a low S/N and a high density of spectral lines. Both problems originate from the nature of these stars. G and K type stars are quite faint and show lots of spectral lines in the optical waveband. If stars have too many lines, the fitting routine may misidentify these lines. This would lead to a shift in the determination of the radial velocity. Furthermore the low S/N, especially for individual spectra, makes it difficult for the programme to distinguish between a "real line" and noise. In order to minimize these errors, each fit was singularly examined carefully, so some false local minima could

⁴<http://wwwuser.oat.ts.astro.it/castelli/colors/sloan.html>

be identified and be fitted again with better start parameters.

4.1.2 Results

As described in Sect. 4.1.1 various fits were made to check if the radial velocities obtained by SSPP and used by Palladino et al. (2014) are reliable. Depending on which starting values and lines were taken for the fit, the velocities obtained here for most average spectra only deviated up to 10 km s^{-1} from the SSPP velocities. Some average spectra showed a bit higher discrepancy to the SSPP values mostly due to low S/N. It is worth mentioning that for Pal18 a radial velocity of about -174 km s^{-1} was obtained whereas SSPP got to $-205.10 \text{ km s}^{-1}$. But after looking at this fit more exactly it seems that it still has a derivation to the spectral lines and therefore the SSPP fit could be the better one.

Furthermore fits for the individual spectra were made to look for variations of radial motion during different epochs. Unfortunately most individual spectra showed very low S/N and therefore obtained values deviated sometimes up to 30 km s^{-1} around the SSPP values.

Yet these variations seemed mostly statistical, whereas it could not be ruled out that the radial velocities were partially caused by a possible binary component of the star. Fortunately the individual spectra of the stars discussed in Sect. 5.2 only show low variations no larger than 20 km s^{-1} . The fit of the individual spectra of Pal18 are more consistent with the SSPP value than the average spectrum.

Altogether we conclude that no major discrepancies to the stellar parameters obtained by SSPP have been found and that no significant sign of binarity can be found. So it seems to be more interesting to check if the proper motions of SDSS can be reproduced.

4.2 Proper Motion

The approach for the measurement of the proper motion is to compare the position of the star on photographic plates (for short: photo plates) of different epochs.

4.2.1 Photographic plates

Since 1950 several sky surveys have been carried out mainly using photographic plates. Those ones were digitized and made available for the public by SuperCOSMOS and the DSS Plate Finder⁵. With the DSS

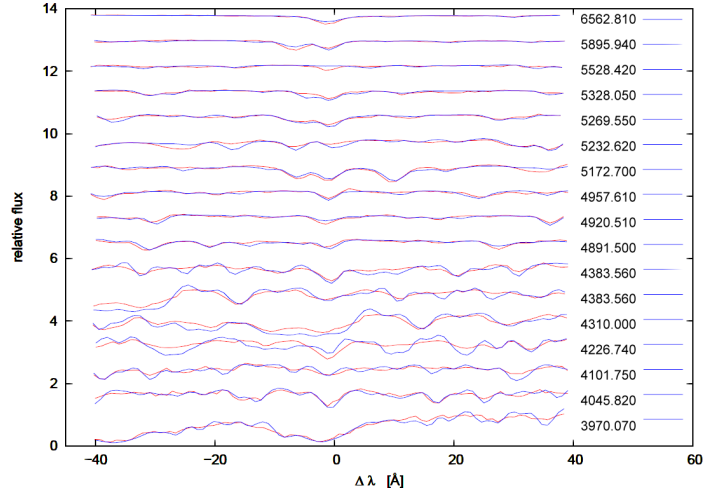


Figure 4.1: Radial velocity fit Pal04:

red: average spectrum of the star, prominent lines are centred and noted at the right in \AA , **blue:** fit on the spectrum, the prominent lines and a range of $\pm 40 \text{\AA}$ around them was fitted.

This fit was obtained by using the stellar parameters of SSPP and only fitting $v_{\text{rad}} = (-50.76 \pm 0.57)[-54.90] \text{ km s}^{-1}$ (the value in square bracket denotes the SSPP value)

⁵https://stdata.stsci.edu/cgi-bin/dss_plate_finder

Plate Finder nearly all available photo plates around a given stellar position can be found.

These archives are great data sources for astronomers. Especially the research on supernovae and on variable stars benefit much from these data over a large time span. Moreover by making use of these archives the proper motions of stars can be determined, as it is carried out in this thesis. The following provides a brief overview of these surveys.

- **POSS I:** The oldest photo plates were taken by the Palomar Observatory Sky Survey in the 1950s with a 1.2m Schmidt telescope covering the northern hemisphere and the equator in its southern extension down to a declination of -33° . A red (POSS-E) and a blue (POSS-O) emulsion were used.
- **POSS II:** In the 1980s the POSS survey was repeated with better photographic plates. In addition to the red and blue plates, a plate in the near infrared was taken.
- **QVN:** Quick-V Northern was a survey of the northern hemisphere in 1970s with low quality photographic plates.
- **UKST:** The 1.2m UK Schmidt Telescope (UKST) provided the southern counterpart of POSS covering $-90 < \delta < +2.5$. It was operated by the Australian Astronomical Observatory. Mainly three emulsions were used⁶:
 - **SERCJ:** Blue emulsion taken between 1979 and 1994
 - **SERCI:** Infrared emulsion taken between 1978 and 2002
 - **Equatorial Red:** Red emulsion taken between 1984 and 1998
- **2MASS:** The Two Micron All Sky Survey is an infra-red survey of the whole sky. Unfortunately on 2MASS plates hardly any star analysed here was visible as the stars are too faint. So no 2MASS plates were used in this work.
- **UKIDSS:** UKIDSS is the newest near-infrared sky survey, the successor to 2MASS. UKIDSS started in 2005 and surveys 7500 square degrees of the northern sky⁷.
- **SDSS:** The Sloan Digital Sky Survey (SDSS) is an automatic photometric and spectroscopic survey providing each area on the sky within the footprint even as a downloadable plate. (see Sect. 3.1)

4.2.2 Procedure

First an 15×15 arcmin field, an extract around the position of the star of all available plates, was downloaded from DSS Plate Finder.

The position of the star has to be determined with respect to a reference background to obtain a reliable position. These background objects have to be exactly at the same place over the entire time span. Therefore it is obvious that these objects have to be far away, so galaxies seem to be a good choice, as they do not move at the available timebase of about 60 years.

To identify galaxies on the plates the SDSS Navigation Tool⁸ was used. SDSS classifies objects by means of photometry and morphology. But one has to be careful, because there is sometimes a misclassification, e.g. very bright red stars are mostly classified as galaxies.

⁶<http://www.roe.ac.uk/ifa/wfau/ukstu/platelib.html>

⁷<http://www.ukidss.org/>

⁸<http://skyserver.sdss3.org/public/en/tools/chart/navi.aspx>

So the galaxies visible in SDSS were compared to the oldest photo-plates. To derive the positions of the galaxies, a 2D-Gaussian fit with the ESO MIDAS Tool CENTER/GAUSS⁹ was made.

The best data can be obtained by very bright nearly point-like galaxies. Unfortunately this is a contradiction in itself. Galaxies are extended objects. The more distant galaxies are, the smaller and more point-like they appear, but they are even getting fainter. Furthermore they can roughly be divided into spiral and elliptical galaxies. The first ones have more inner structure than the second ones. The consequence is that the maximum of intensity, which defines the position of the object, can be better determined for elliptical galaxies than for spiral ones.

Moreover the intensity maximum of the galaxy lies at different spectral wavelength, i.e. in different filters, at slightly different positions. For example the spiral arms appear blue and the bulge appears more red.

Apart from that the best reference objects would be quasars, unless they weren't so rare. These are very distant, extremely bright objects powered by an Active Galactic Nucleus (AGN), which outshines the whole host galaxy.

The best way to minimise all these errors is to use a large sample of galaxies. While doing the coordinate-fit of each star, galaxies which seem to be too far away of their original positions, have to be excluded from this fit. Otherwise they would distort the result. Finally the position of the star from each plate was plotted and the proper motion was fitted.

4.2.3 Results

In some low Galactic latitude fields it was very difficult to find enough Galaxies for a reliable fit. This can be explained by the higher density of stars and interstellar matter (ISM) in the direction of the Galactic disk. This higher density causes the major extinction of the light of distant galaxies compared to the direction which is perpendicular to the disk. Pal05, Pal07, Pal08 and Pal10 remarkably show this effect. Moreover Pal07 and Pal08 are at the edge of the SDSS footprint, which is the name for the area on the sky, for which SDSS took data.

Furthermore at least one POSS I plate should be taken for each fit to get a sufficiently large time line. Yet sometimes there was another star very near the candidate so that it was impossible for MIDAS to separate the two stars on older plates. This was the case for Pal01 and Pal11.

Taking the considerations above into account, rather reliable proper motions could be obtained for 14 of the 20 candidates. Depending on the field 16 to 29 galaxies were found per plate. Pal17 and Pal 20 showed too few galaxies in a field of 15×15 arcmins, so a larger field of 20×20 arcmins had to be chosen.

As an example, relative positions of each photo plate for Pal15 are shown in figure 4.2. A linear regression was made to obtain the proper motion of the star. By this example the features of the different photo plates are discussed, for further proper motion fits see Appendix C.

POSS I covers the biggest part of the sky, so a POSS I plate can be found for every SDSS object, whereby not every plate can be used, because of the low resolution (see above). As seen in figure C.1 positions derived from QVN (Quick-V Northern)(QUICK) had the largest error bars of all plates and were mostly not on the fit. All UKST plates (SERCJ,SERCI,Equatorial Red) and POSS II plates delivered quite good data. Unfortunately the UKST plates were only available for few fields near the equator, because UKST is a survey of the southern hemisphere. The SDSS plates predominantly have very small error bars with one exception: The u-filter-plate shows a very low intensity and has therefore huge errors in determination of

⁹<http://www.eso.org/sci/software/esomidas/>

position of an object. Furthermore mainly all SDSS plates for a specific star are nearly of the same epoch, hence it is remarkable that there are three epochs of SDSS observations for Pal 18. Moreover for very few stars there were even plates of UKIDSS. UKIDSS delivers the newest plates with the highest resolution, as it becomes obvious from the small error bars. Eventually it should be mentioned that sometimes the position determination seems to have a larger error than estimated.

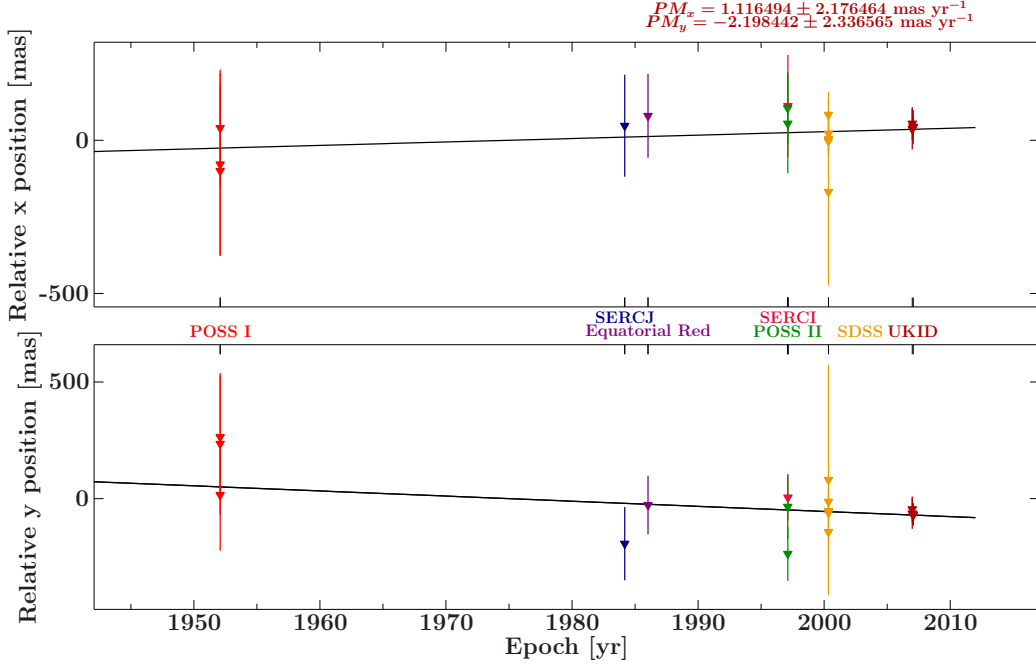


Figure 4.2: Propermotion Measurement Pal15:

The relative positions of the star from each photo plate was plotted and a linear regression was made to obtain the proper motion of the star.

For every star an error weighted and a straight (non-error weighted) proper motion fit was made. The obtained values are all lower than the proper motions obtained by SDSS, as can be seen in table 4.1.

This may be caused by the fact that automatic systems like SDSS are not as good as the human eye in detecting patterns, so the automatic systems may have mixed up stars when comparing positions at different epochs. If two stars are very close to each other, it may be possible that such a misidentification occurs. As Palladino et al. (2014) made some checks in that matter, the errors of SDSS have been obviously underestimated.

Pal04

Pal04 is the most extreme case and should be discussed shortly. In the sample of Palladino et al. (2014) Pal04 was outstanding as the brightest star (16.15 mag), the smallest distance to the sun (1.04 kpc) and the highest velocity (1296.7 km s^{-1}). Because of its brightness and closest distance one should think that the obtained data are very reliable. Indeed the spectrum of Pal04 (see Figure 4.1) is very clean and the area around the star is free of stars, which could lead to a misidentification. Yet the proper motion obtained in this thesis $\mu_\alpha \cos(\delta) = -12.9 \text{ mas yr}^{-1}$, $\mu_\delta = -20 \text{ mas yr}^{-1}$ and is therefore significantly lower than that of SDSS, PPMXL, Nomad and USNO, even the direction of μ_δ is reversed (see table 3.2 and table 3.2). But the entry

Table 4.1: proper motions obtained in this work in comparison to SDSS

Pal	error	weighted	non-error	weighted	SDSS	
	$\mu_\alpha \cdot \cos(\delta)$	μ_δ	$\mu_\alpha \cdot \cos(\delta)$	μ_δ	$\mu_\alpha \cdot \cos(\delta)$	μ_δ
2	8.9±4.7	8.6±3.7	12.0±6.6	8.6±5.8	-2.6 ± 3.0	15.5 ± 3.0
3	5.5±4.0	-10.4±4.7	6.1±4.0	-8.5±1.9	23.6 ± 3.0	-1.6 ± 3.0
4	-12.9±2.4	-20.0±4.1	-16.6±2.0	-23.2±1.8	-117.2 ± 5.9	206.8 ± 5.9
6	5.8±2.2	-4.5±2.5	9.0±2.3	-5.2±2.5	-41.6 ± 5.5	20.1 ± 5.5
9	-3.1±3.1	-8.5±3.2	-2.3±0.5	-4.8±1.9	4.8 ± 2.9	-65.3 ± 2.9
12	7.3±2.6	21.4±2.9	7.4±2.7	22±4.2	19.4 ± 2.8	38.1 ± 2.8
13	-2.0±2.5	-5.6±2.7	-4.9±5.5	-3.4±1.8	39.6 ± 3.0	-19.1 ± 3.0
14	-0.9±2.9	-1.3±2.4	-4±2.6	0.3±2.0	-5.7 ± 3.9	-44.5 ± 3.9
15	1.1±2.2	-2.2±2.3	1.4±0.9	-4.2±1.3	-58.6 ± 5.4	8.1 ± 5.4
16	-5.2±4.6	1.1±5.1	-4.3±2.9	1.0±1.4	0.8 ± 5.7	-58.1 ± 5.7
17	12.5±3.2	13±3.5	6.4±2.6	11.9±1.9	25.2 ± 2.5	42.1 ± 2.5
18	1.8±2.3	-28.6±3.5	0.7±1.7	-27.5±3.1	7.2 ± 3.1	-32.2 ± 3.1
19	-9.0±2.0	-2.8±1.7	-8.8±5.9	-2.5±2.4	-28.8 ± 6.9	8.7 ± 6.9
20	-0.4±2.4	-1.0±3.1	7.0±5.1	-4.5±4.6	15.4 ± 5.8	-5.8 ± 5.8

$\mu_\alpha \cos(\delta) = -17.5 \text{ mas yr}^{-1}$, $\mu_\delta = -19.5 \text{ mas yr}^{-1}$ of the UCAC4 catalog conforms to our measurement.

Comparison between consistency of Measurements

For illustration of these values the tangential velocity v_t was plotted against the radial one v_r as done by Palladino et al. (2014) (See therefore figure 3.1 and sec. 1.4). In figure 4.3 only stars for which proper motions could be obtained in this work are plotted. A normal distribution of stars is described by a $\sqrt{2}$ times higher v_t than v_r as displayed by the red line. As it can be seen, the new values for the stars are characterized by significantly lower transverse velocity in comparison to the SDSS values used by Palladino et al. (2014). This is a bit more like a normal distribution of stars indicating that the proper motions obtained in this work are consistent. But one star, Pal18, possesses an outstanding high radial and tangential velocity in comparison to all other stars. Furthermore two other stars, Pal02 and Pal12, show quite a high ratio of v_t/v_r .

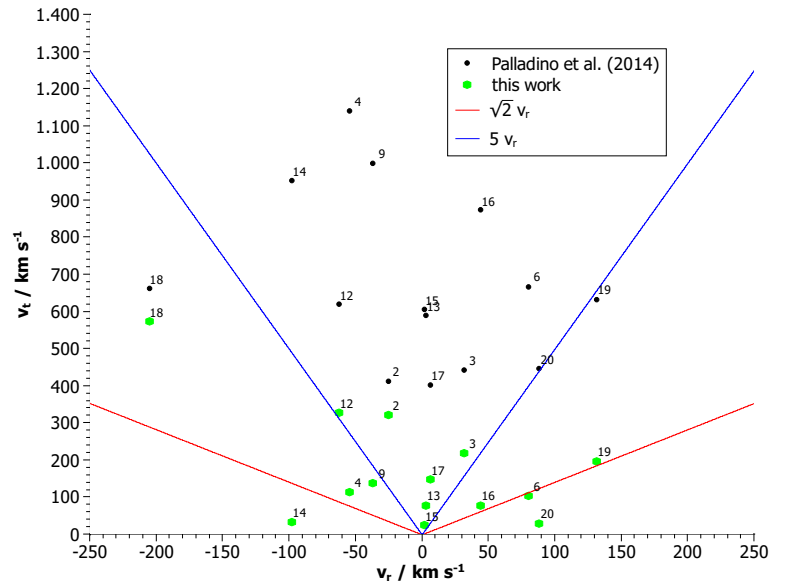


Figure 4.3: Ratio of transverse to radial velocity

The filled black circles are from Palladino et al. (2014) and green Hexagons are from this work. A normal distribution of stars is described by a $\sqrt{2}$ times higher v_t than v_r as displayed by the red line.

Furthermore two other stars, Pal02 and Pal12, show quite a high ratio of v_t/v_r .

Chapter 5

Analysis of Orbits

5.1 Calculation of bound-probability

Pal	Palladino et al.	SDSS			Initial Gaia			this work I	this work II	this work III
		I	II	III	I	II	III			
1	6.35	0.95	0.20	44.37	3.84	1.2	51.07			
2	7.43	23.23	10.84	94.38	97.89	95.56	100	92.12	84.29	99.90
3	34.88	48.74	33.68	96.18	97.98	95.73	99.95	99.99	99.88	100.00
4	0.00	0.08	0.01	0.87	100.00	100	100	100.00	100.00	100.00
5	0.04	0.00	0.00	0.09	0.00	0	0.04			
6	0.07	1.14	0.29	19.82	0.05	0.03	1.4	100.00	100.00	100.00
7	0.30	2.22	0.78	47.76	5.43	2.19	56.28			
8	1.01	8.93	4.26	67.85	31.39	18.49	89.6			
9	1.20	3.31	1.94	23.04	5.98	3.67	32.01	100.00	100.00	100.00
10	1.34	3.09	1.83	20.11	6.21	4.06	32.63			
11	2.89	1.37	0.17	85.65	51.34	34.36	98			
12	3.77	10.88	5.47	68.59	74.28	60.96	98.98	91.63	81.37	99.98
13	4.42	16.80	9.43	79.88	61.21	44.81	97.37	100.00	100.00	100.00
14	5.86	10.88	6.86	43.11	100.00	99.99	100	100.00	100.00	100.00
15	15.98	33.70	21.28	88.60	23.29	14.68	79.44	100.00	100.00	100.00
16	19.70	23.06	12.08	83.87	94.05	88.33	99.94	99.97	99.96	100.00
17	20.01	44.33	43.62	44.86	70.74	70.5	99.99	100.00	100.00	100.00
18	21.30	41.68	30.35	87.58	68.56	59.51	95.23	74.45	64.17	97.77
19	23.69	43.43	34.23	80.18	26.63	21.35	57.79	100.00	100.00	100.00
20	43.24	52.61	43.43	85.74	12.52	9.58	39.74	100.00	100.00	100.00

Table 5.1: bound-probabilities [%] of different proper motion catalogs and in different potentials: The bound-probability is defined as the number of possible orbits not exceeding the local escape velocity in respect to the number of all calculated possible orbits. Bound-probabilities obtained by Palladino et al. (2014) are listed in comparison to bound-probabilities obtained with proper motions of SDSS, Initial Gaia list and this work. The Roman numbers stand for the different potential models used (see Sect. 2.2).

Originally HVSs were defined as stars unbound to the galaxy, hence it is worthwhile to calculate the probability of each star of being bound for different proper motion measurements and galactic potentials.

Therefore the velocity was transformed into Galactic coordinates (see Sect. 2.1) and a Monte Carlo (MC) simulation was used to calculate 10000 possible orbits varying all parameters within their errors. This MC-simulation was written by Irrgang et al. (2013) and was named "orbit calculator". In order to gain the bound probability, the number of orbits with higher kinetic energy E_{kin} than potential Energy E_{pot} was evaluated (see Sect. 2.3). The result is shown in table 5.1. Only by taking the same proper motions as Palladino et al. (2014) took other, mainly higher values are obtained. The results for the Gaia initial list indicate that many of these stars are actually more tightly bound to the Galaxy than suggested by Palladino et al. (2014). Finally, by taking the proper motions obtained in this work, nearly all stars are bound, only Pal02, Pal12 and Pal18 have a non-vanishing probability of being unbound. Model III, Navarro-Frenk-White-Profile, shows the highest bound-probabilities due to its high halo mass.

5.2 Interesting Candidates

As it can be seen in table 5.1 three of the stars still have a non-vanishing probability of being unbound and therefore are still HVS candidates. These candidates should be discussed in more detail. For this issue only potential model I (Allen & Santillan (1991)) is used and the MC simulation traced back 5 Gyr to determine their possible origin.

5.2.1 Pal02

The v_{GRF} obtained by the 10000 runs of the MC simulation of the current stars' state was binned in steps of 20 km s^{-1} and plotted in figure 5.1. The average velocity and velocity standard deviation is calculated to be $424.20 \pm 100.63 \text{ km s}^{-1}$ (see table A.7) and the gray area indicates the range of velocities which are lower than the escape velocity ($v_{\text{esc}} = 565.06 \pm 4.46 \text{ km s}^{-1}$) and the star is therefore bound. The error of the escape velocity, resulting from the uncertainty of distance determination of the star, is lower than the Histogram's steps.

For making a statement about the orbits of the stars the MC runs were traced back 5 Gyr. The calculation was stopped when the star crossed the disk within 100 kpc distance to the GC. Orbits with disk crossings were separated from orbits without ones. The results were plotted in comparison to the structure of the Galaxy (see figure 5.2 and so on). The black dot in the middle illustrates the SMBH, the asterisk stands for the position of the sun at a distance of 8.33 kpc away from the GC and the circle is the Galactic disk with a radius of 30 kpc in the

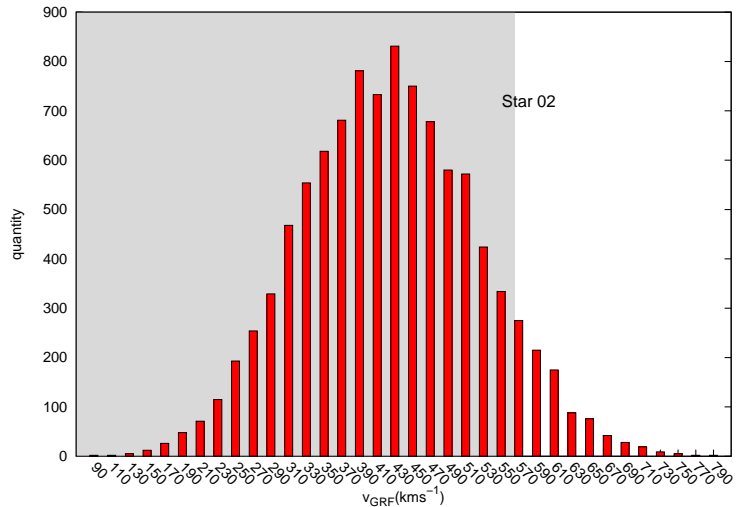


Figure 5.1: Pal02: Velocity Histogram of possible velocities obtained by 10000 runs if the MC simulation with potential model I. The gray area indicates the range of velocities which are lower than the escape velocity. ($v_{GRF} = 424.20 \pm 100.63 \text{ km s}^{-1}$, $v_{\text{esc}} = 565.06 \pm 4.46 \text{ km s}^{-1}$)

x-y-plane. The crossing points were binned and colour coded. Narrow lines around the bins indicate the 1σ area and bold lines demonstrate the 3σ area of the data.

Figure 5.2 shows such a diagram for Pal02 with disk passages within 100 kpc. The distribution of crossing points is spread over a large area, because of high uncertainties in velocity determination. The maximum of the distribution lies outside the disk, indicating an origin in the stellar halo, e.g. in a globular cluster or in a satellite galaxy. The time where the crossing happened was $t = (949 \pm 958)$ Myr ago. Yet it may be even possible that the star was not ejected during this x-y-plane crossing, because the star can live long enough to have done more than one of such crossings.

So as seen in Figure 5.3 a second calculation was carried out. This time it was only stopped when a passage within 30 kpc occurred. Now it can indeed be seen that some of the x-y-passages in previous figures' outer regions had already disk passages ~ 800 Mio. years earlier within 30 kpc on the opposite side of the galaxy (right clump: $t = (997 \pm 400)$ Myr ago, left clump: $t = (1787 \pm 1904)$ Myr ago). But there is no evidence for an origin in the neighbourhood of the SMBH, so the origin in the halo or outer disk is still favoured.

At this point it should be mentioned that all possible orbits crossing the x-y-plane within 100kpc are bound orbits for all stars in this sample. So if these stars originate from the disk or bulge, they are definitely bound. Only if some stars of the sample come from outer regions like globular clusters or satellite galaxies, they may be unbound.

For visualisation of the above disk crossings, the orbit of the star from 1850 Myr ago (blue) to 500 Myr (red) to the future was plotted without any error considerations (see figure 5.4).

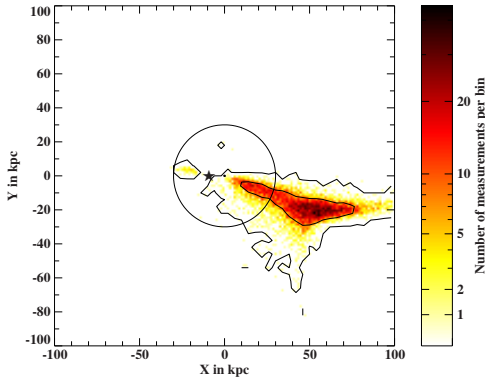


Figure 5.2: Pal02: possible Origins obtained by 10000 MC runs stopped when a Galactic disk passages within 100kpc happened. The number of possible crossings was binned and colour coded.

Black dot: GC,
circle: Galactic disk with radius 30 kpc,
Asterisk: Sun

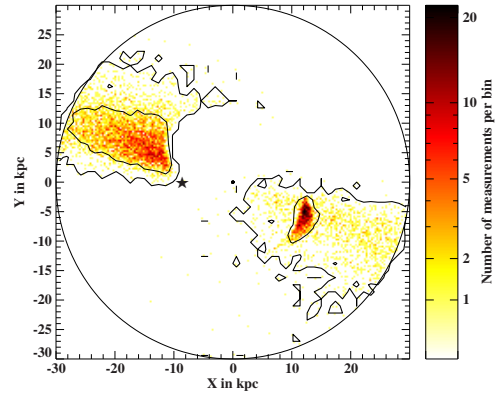


Figure 5.3: Pal02: possible Origins - Galactic disk passages within 30kpc, analogous to figure 5.2,
right clump: last disk crossing,
left clump: second last disk crossing about 800 Myr earlier

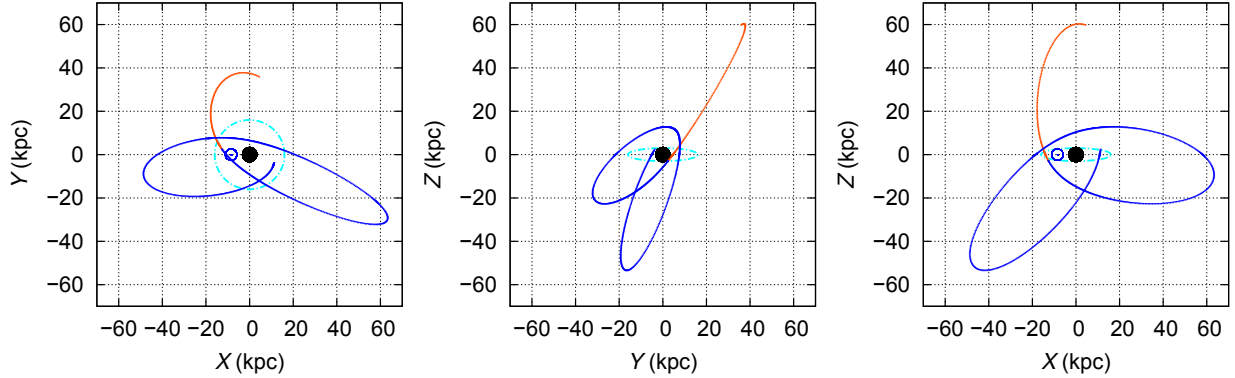


Figure 5.4: Pal02: 2D-projection of Orbit without error consideration. The plotted **time line** is from 1850 Myr ago (blue), where the second last disk crossing happened till 500 Myr in the future (red). **Black dot:** GC, **light blue circle:** Galactic disk with radius 30 kpc, **dark blue circle:** Sun

5.2.2 Pal12

Similar to Pal02 a velocity histogram, disk passage diagrams and an orbit plot were made. Pal12 owns a velocity of $483.70 \pm 69.98 \text{ km s}^{-1}$.

Unlike Pal02 the disk origin distribution is given by a quite small area in a distance of 20 to 30 kpc from the GC (see figure 5.6). This could be an indication for an ejection out of the galactic disk by a supernova of a former binary component for example. But the star could alternatively be just a normal halo object crossing the disk several times. The time when the last disk encounter happened was about $t = (1517 \pm 989) \text{ Myr}$ ago.

The orbit plots (figure 5.8 and figure 5.7) give more confidence about the conclusion taken by figure 5.6.

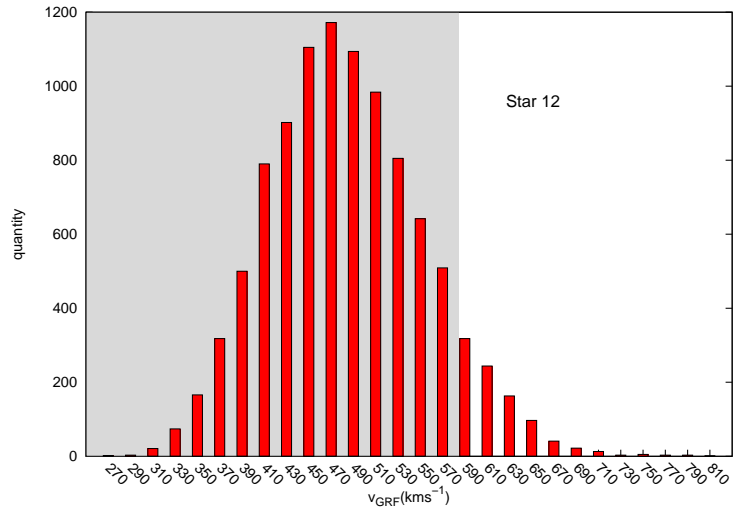


Figure 5.5: Pal12: Velocity Histogram (for explanation see fig 5.1, $v_{GRF} = 483.70 \pm 69.98 \text{ km s}^{-1}$, $v_{esc} = 584.01 \pm 2.80 \text{ km s}^{-1}$)

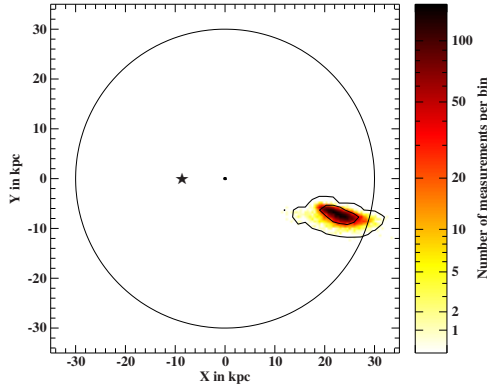


Figure 5.6: Pal12: possible Origins - Galactic disk passages within 100kpc, analogous to figure 5.2

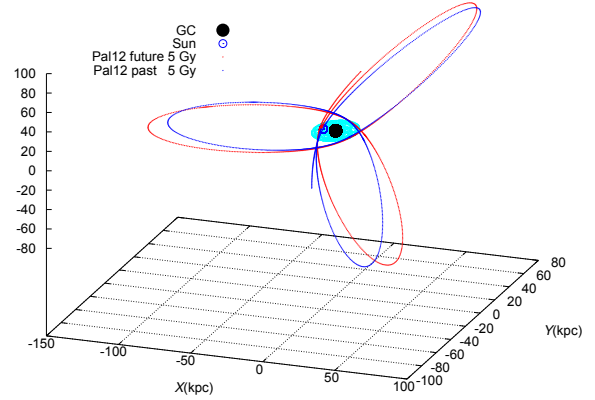


Figure 5.7: Pal12: Orbit 3D, analogous to figure 5.4, **time line:** from -5 Gyr Myr (blue) to 5 Gyr (red)

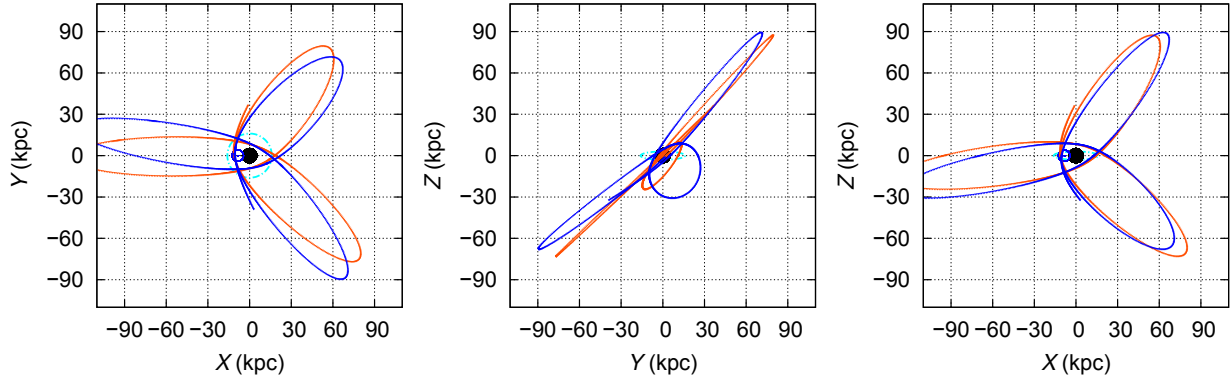


Figure 5.8: Pal12: Orbit 2D-projection, analogous to figure 5.4, **time line:** from -5 Gyr Myr (blue) to 5 Gyr (red)

5.2.3 Pal18

The same figures as for the previous examples were plotted again for Pal18.

Pal18 with $537.57 \pm 123.16 \text{ km s}^{-1}$ has the highest velocity of the examined sample and therefore is the most promising candidate. But its velocity dispersion is broader and therefore the binning in figure 5.9 was made in steps of 30 km s^{-1} . As illustrated in 5.10 the most probable origin of Pal 18 is an area which is only 2 kpc away from the GC. The black circle around the GC indicates a radius of 0.6 kpc around the GC to get an impression how near the distribution to the GC is. So Pal18 is in accord with being accelerated by the SMBH within the error range. This makes Pal18 a candidate for the Hill's mechanism. Note that the outer ring in this case signals the Galactic disk within 10 kpc. If Pal18 was not accelerated by the SMBH, it might be that multi-body interactions with the dense stellar environment in the inner regions of the Galaxy could have catapulted Pal18 on the highly eccentric orbit seen in figures 5.12, 5.13 and 5.14. Pal18 reaches distances of up to 150 kpc to the GC and then comes back again for a close encounter with the GC. Remember that orbits passing the disk and the GC are bound orbits for this sample of stars, as mentioned in section 5.2.1.

So if Pal18 really originates from the GC, bulge or disk, it is definitely bound. The last disk crossing took place about $t = (1289 \pm 1059)$ Myr ago.

In figure 5.11 the possible origin from orbits without any x-y-plane encounter within 100kpc is displayed. Therefore the calculated position of the star 5 Gyr ago was taken and projected in the x-y-plane. Note that the steps on the x-axis are bigger than on y-axis and that the Galaxy is located in the lower right edge of the diagram. The upper right black dot denotes the position of the Andromeda Galaxy (M31). As seen from the distribution, an origin in M31 seems to be very unlikely though that would be very interesting. Sherwin et al. (2008) analysed mechanisms in M31 that could accelerate stars in the direction of the Milky Way. They concluded that there should be roughly one thousand low mass stars, like Pal18, in the halo of the Milky Way originating from M31. But the calculation up to such high distances, made here, should be taken with caution, because the potential model of Irrgang et al. (2013) cuts off at 200 kpc and is therefore not valid in this range.

Yet apart from these speculations it should even be kept in mind that Pal18 has the second lowest metallicity ($[\text{Fe}/\text{H}]$) and the highest α -enrichment ($[\alpha/\text{Fe}]$) of the sample. These are signs for a origin in the thick disk or the halo.

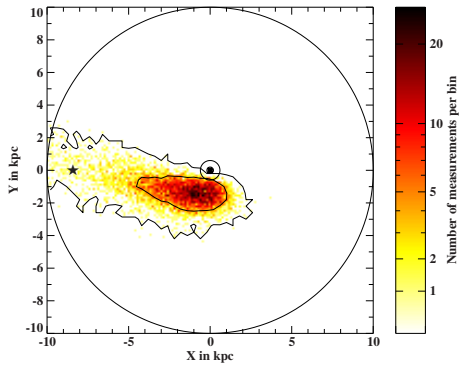


Figure 5.10: Pal18: possible Origins - Galactic disk passages within 100kpc, analogous to figure 5.2, **inner Black circle:** radius 0.6 kpc around the GC, **circle:** Galactic disk with radius 10 kpc

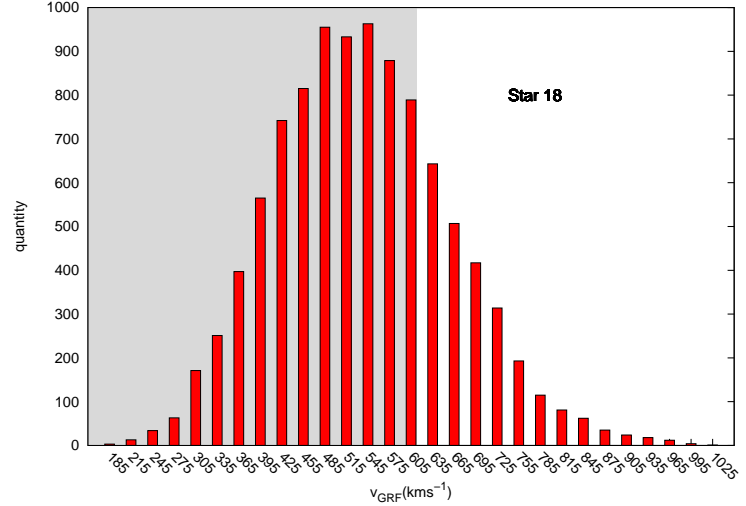


Figure 5.9: Pal18: Velocity Histogram (for explanation see fig 5.1, $v_{GRF} = 537.57 \pm 123.16 \text{ kms}^{-1}$, $v_{esc} = 612.58 \pm 4.50 \text{ kms}^{-1}$)

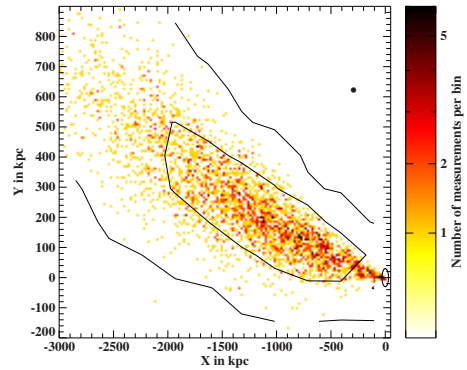


Figure 5.11: Pal18: possible Origins projection on disk - without a Galactic disk passage within 100kpc, analogous to figure 5.2, **right bottom corner:** Milky way, **upper right black dot:** M31

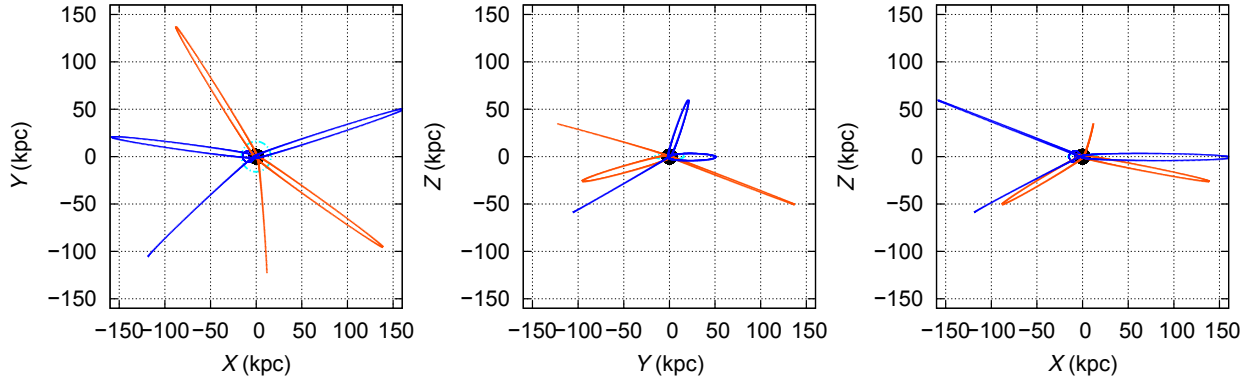


Figure 5.12: Pal18: Orbit 2D-projection, analogous to figure 5.4, **time line:** from -5 Gyr Myr (blue) to 5 Gyr (red)

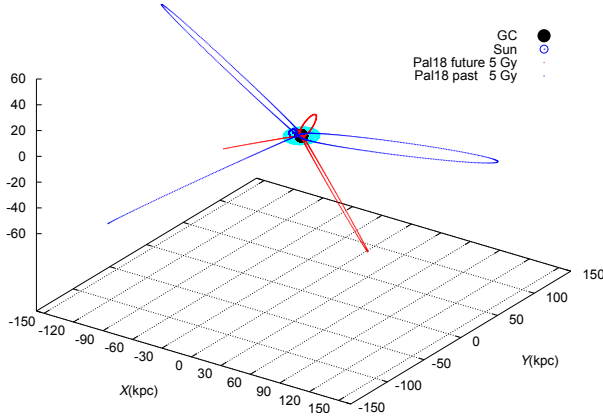


Figure 5.13: Pal18: Orbit 3D, analogous to figure 5.4, **time line:** from -5 Gyr Myr (blue) to 5 Gyr (red)

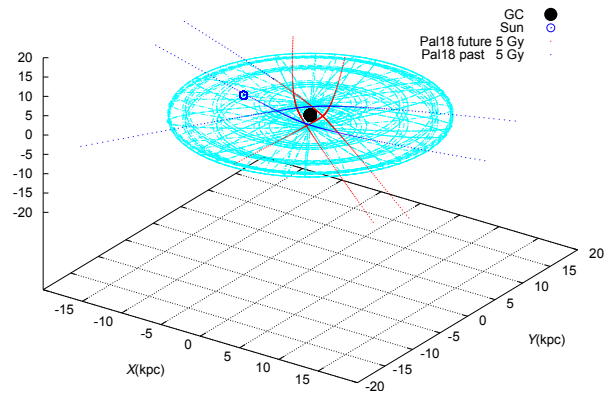


Figure 5.14: Pal18: Orbit 3D - zoom in version of figure 5.13

5.3 Kinematic properties

As we saw above, all but one star are apparently no HVSs, so it is interesting whether it can be confirmed that they are population II stars, i.e. indigenous halo stars. Therefore their kinematic properties were investigated more closely.

Analogical to Pauli et al. (2006) a U-V-Diagram (see figure 5.16) was created with U indicating the Galactic radial velocity and V the Galactic rotational component. The numbered dots with error bars represent the stars examined in this work in relation to the white dwarfs analysed by Pauli et al. (2006). The dashed line indicates the 3σ range of the thick disk, whereas the solid line indicates the range of the thin disk. Objects outside this area belong to the halo. As one can see Pal19 and Pal02 could belong to the thick disk within the error range. All other stars obviously belong to the halo. Furthermore seven stars show negative V-values and are therefore on retrograde orbits. Again Pal18 distinguishes from all others.

Sakamoto et al. (2003) set limits to the mass of the Galaxy by requiring 11 satellite galaxies, 137 globular clusters and 413 field horizontal-branch stars (FHB) to be bound to the Galaxy. Now this sample can be used to compare other stars with them to get an overview whether stars belong to the halo or do show significant difference to other halo objects. In figure 5.17 v_{GRF} was plotted over the distance r of the star to the GC. Obviously the examined stars are widely similar to the sample of Sakamoto et al. (2003) and are therefore most likely indigenous halo stars. Only the above extensively discussed stars (Pal02, Pal12 and Pal18) are at the edge of the sample.

Even the Orbits are most like orbits of Halo stars, which can especially be well seen in figure 5.15.

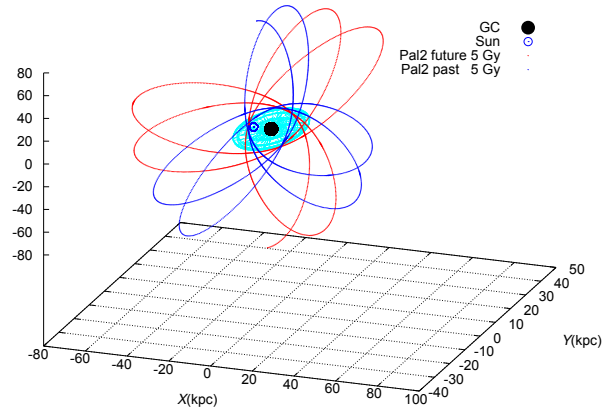


Figure 5.15: Pal02: Orbit 3D, analogous to figure 5.4, **time line:** from -5 Gyr Myr (blue) to 5 Gyr (red)

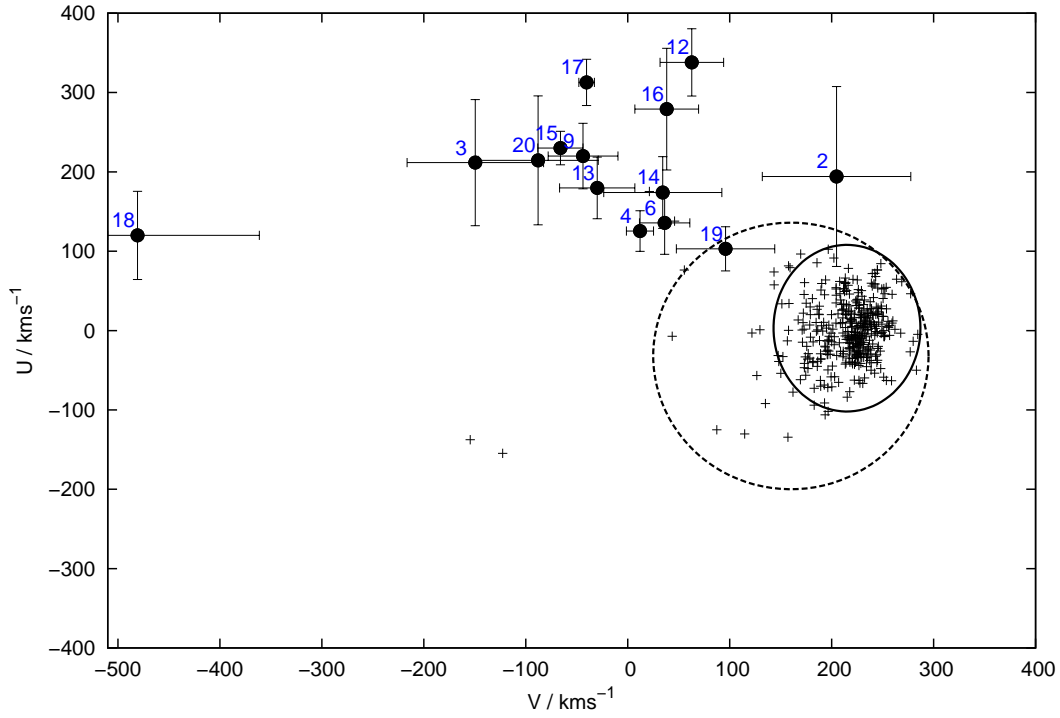


Figure 5.16: U-V-Diagram, **numbered dots with error bars:** stars examined in this work, **black crosses:** white dwarfs analysed by Pauli et al. (2006), **dashed line:** 3σ range of the thick disk, **solid line:** 3σ range of the thin disk, **Objects outside this area:** belong to the halo.

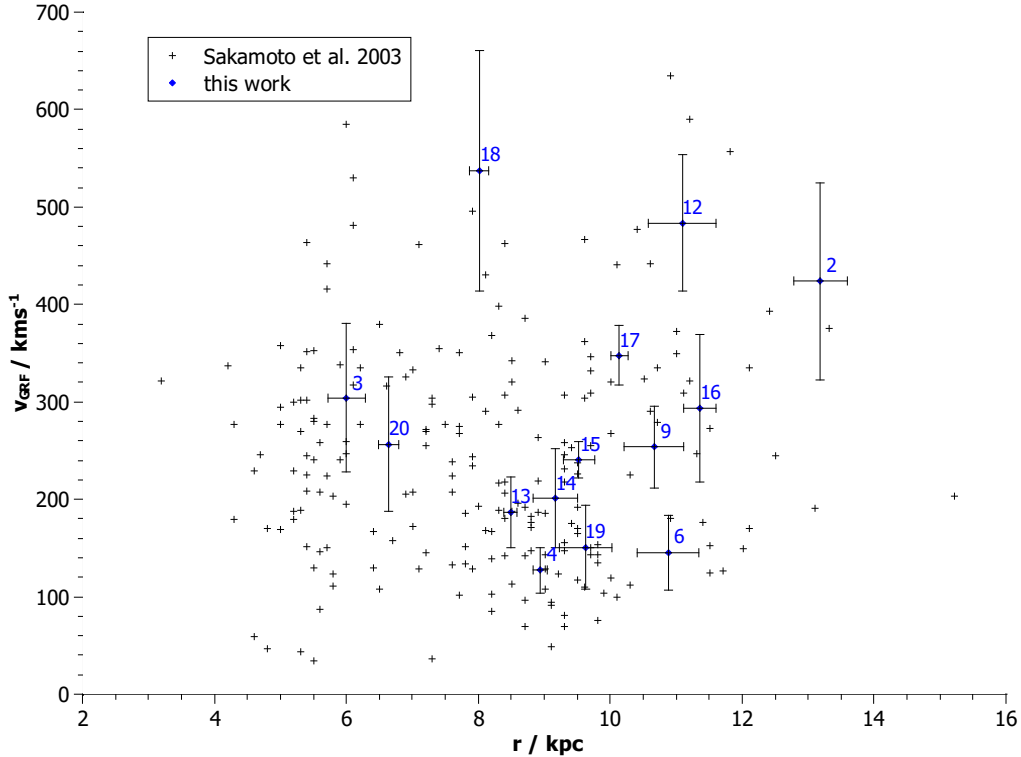


Figure 5.17: examined stars (numbered dots with error bars) in comparison to the sample of Sakamoto et al. (2003) (11 satellite galaxies, 137 globular clusters and 413 field horizontal-branch stars)

Chapter 6

Conclusion and Outlook

A sample of 20 stars supposedly low mass Hypervelocity stars (HVSs) by Palladino et al. (2014) was analysed more closely. Theoretical estimations of Kenyon et al. (2014), the abnormal high proper motions listed in SDSS data base, the deviating proper motion values found in various catalogs, and especially the low metallicity of the stars gave rise to doubt the results of Palladino et al. (2014). The radial velocities of the sample could be confirmed, whereas the proper motions, derived for 14 stars of the sample, were significantly lower than in SDSS. A plot of transverse velocity against radial velocity proves the higher consistency of these proper motion measurements compared to the SDSS data base. Moreover Kenyon et al. (2014) notes that the sample of Palladino et al. (2014) would only suit to their models, if the proper motions were reduced by a factor of 5.

After that their Galactic rest frame (GRF) velocity was calculated in three potential models of the Galactic gravitational field. Only 3 of 14 stars remain with a non-vanishing probability of being unbound. Furthermore only one star, Pal 18, shows such an extreme orbit that it might originate from the GC. But it should even be noted that all possible orbits with x-y-plane crossings within 100kpc during the last 5 Gyr are bound orbits for these stars. A comparison to the white dwarf sample of Pauli et al. (2006) and the field stars of Sakamoto et al. (2003) reveals that most of the stars are most likely normal halo stars, as their low metallicity has already hinted at.

Apart from Palladino et al. (2014) even other authors reported surveys for low mass HVS candidates. The only star in the sample of Li et al. (2012) which has such a high velocity that it is definitely unbound shows a suspiciously high proper motion. Whereas the star sample Zhong et al. (2014) seems quite reliable due to their comparison of the obtained proper motions with PPMXL and UCAC4. But it is unclear whether Zhong et al. (2014) and Li et al. (2012) suffer from analogous misidentification as Palladino et al. (2014), due to incorrect proper motion measurements. Thus this point would be worth to be investigated further. Yet the method of proper motion determination used in this work is very time consuming and therefore unsuitable for large samples of stars. The Gaia satellite, the successor of the Hipparchos satellite, was launched in December 2013 and has been operating since July 2014, will provide considerably more reliable proper motions than ground based surveys in a few years. So this subject will stay interesting and maybe in the near future we will be able to answer the question, if there are as many low mass HVS as supposed by applying the Salpeter initial mass function to the Galactic Center or if we still do not understand how stars are ejected out of the Galaxy.

Appendix A

Orbit Calculator Tables

The following tables are the result of statistical analysis of the parameters obtained by orbit simulation with the programme "orbit calculator" of Irrgang et al. (2013). v_{av} denotes the average v_{GRF} , v_{min} is the minimal v_{GRF} , v_{max} is the maximal v_{GRF} and v_{sdev} is the standard deviation of this. E represents the total energy, if it is negative, the orbit is bound (see Sect. 2.3).

Table A.1: Orbit parameters using SDSS obtained μ and Model I

Pal	v_{av}	v_{min}	v_{max}	v_{sdev}	E_{av}	E_{sdev}	U_{av}	U_{sdev}	V_{av}	V_{sdev}	Bound %
1	803.54	458.67	1193.16	92.30	0.1606	0.0794	345.84	37.04	-612.03	82.27	0.95
2	637.25	356.89	977.90	86.54	0.0455	0.0593	100.26	49.50	539.79	80.77	23.23
3	648.71	351.16	1148.74	97.36	0.0109	0.0668	-124.78	43.42	562.70	81.87	48.74
4	1307.11	386.71	2096.91	214.53	0.7234	0.2971	655.05	134.58	784.04	99.14	0.08
5	1093.87	804.96	1466.94	86.05	0.4189	0.0987	869.43	94.48	507.32	22.46	0.00
6	921.87	419.45	1586.96	150.31	0.2744	0.1514	-88.13	63.47	854.42	138.63	1.14
7	798.08	364.43	1199.67	105.07	0.1588	0.0914	66.54	12.15	786.16	102.46	2.22
8	772.97	406.35	1330.09	110.60	0.1126	0.0901	357.32	87.57	482.19	26.65	8.93
9	939.96	315.96	1755.22	186.82	0.2968	0.1896	-180.73	51.99	-175.78	77.74	3.31
10	998.55	261.96	1788.19	200.63	0.3248	0.2123	-699.60	148.41	-17.22	46.57	3.09
11	719.69	476.91	981.83	63.98	0.0952	0.0495	47.54	19.49	633.02	57.61	1.37
12	736.91	347.61	1213.58	117.01	0.1098	0.0945	184.43	50.24	351.00	43.61	10.88
13	718.09	343.03	1132.59	108.94	0.0809	0.0843	-574.02	106.64	416.69	52.93	16.80
14	840.32	189.06	1614.04	193.31	0.1984	0.1778	-709.92	171.92	-156.82	66.63	10.88
15	656.38	283.03	1141.07	117.33	0.0426	0.0844	469.49	99.45	312.01	52.49	33.70
16	675.25	279.00	1141.10	114.80	0.0654	0.0835	-110.60	38.92	-592.18	109.65	23.06
17	604.14	472.18	769.61	37.72	0.0045	0.0246	-94.08	8.98	493.87	28.90	44.33
18	650.11	234.92	1250.35	133.47	0.0320	0.0952	-543.75	118.63	188.89	75.38	41.68
19	645.25	94.66	1545.73	186.42	0.0477	0.1378	551.52	169.46	295.78	126.54	43.43
20	628.96	80.66	1545.54	178.33	0.0176	0.1281	-430.09	148.84	380.51	164.32	52.61

Table A.2: Orbit parameters using SDSS obtained μ and Model II

Pal	v_{av}	v_{min}	v_{max}	v_{sdev}	E_{av}	E_{sdev}	U_{av}	U_{sdev}	V_{av}	V_{sdev}	Bound %
1	805.51	487.19	1129.29	92.03	0.1876	0.0794	345.39	37.01	-614.29	81.99	0.20
2	635.36	303.24	1003.32	87.17	0.0695	0.0596	100.30	49.63	537.63	80.75	10.84
3	646.04	342.32	1079.24	98.09	0.0348	0.0670	-125.61	43.55	559.78	81.83	33.68
4	1308.82	507.14	2396.11	212.31	0.7508	0.2954	656.48	132.84	783.88	98.42	0.01
5	1092.85	790.97	1455.57	85.31	0.4434	0.0976	869.22	93.80	506.30	22.36	0.00
6	925.31	460.71	1584.82	147.33	0.3027	0.1493	-89.55	64.55	856.90	135.96	0.29
7	796.71	452.67	1256.91	105.69	0.1830	0.0918	66.53	12.13	784.76	103.11	0.78
8	772.24	391.77	1245.74	111.22	0.1378	0.0903	357.67	88.31	480.84	26.94	4.26
9	938.95	268.17	1663.46	187.64	0.3214	0.1900	-180.13	52.33	-177.65	78.09	1.94
10	993.39	329.15	1766.42	196.59	0.3444	0.2069	-696.00	145.73	-19.27	45.06	1.83
11	716.48	499.83	952.89	64.18	0.1181	0.0494	47.65	19.68	629.91	58.10	0.17
12	738.10	344.03	1197.73	117.74	0.1362	0.0952	184.91	50.66	349.87	43.97	5.47
13	715.68	340.86	1213.83	111.03	0.1049	0.0858	-571.92	108.14	415.51	53.98	9.43
14	846.35	180.10	1750.61	196.50	0.2300	0.1833	-715.00	174.57	-159.11	67.70	6.86
15	655.46	309.15	1325.53	117.36	0.0675	0.0849	469.42	99.37	309.59	51.76	21.28
16	677.29	319.54	1148.87	114.38	0.0921	0.0838	-110.45	38.80	-594.43	109.49	12.08
17	603.24	466.57	773.08	37.67	0.0294	0.0246	-94.09	9.06	492.80	28.65	11.21
18	648.95	212.48	1256.20	135.04	0.0571	0.0961	-543.25	120.53	187.52	75.81	30.35
19	646.85	122.16	1571.79	188.47	0.0748	0.1400	553.32	171.86	296.25	125.61	34.23
20	629.80	87.90	1545.06	180.92	0.0443	0.1302	-431.23	150.02	379.78	166.49	43.43

Table A.3: Orbit parameters using SDSS obtained μ and Model III

Pal	v_{av}	v_{min}	v_{max}	v_{sdev}	E_{av}	E_{sdev}	U_{av}	U_{sdev}	V_{av}	V_{sdev}	Bound %
1	805.33	465.81	1165.55	90.87	0.0165	0.0785	345.97	37.49	-614.60	81.17	44.37
2	634.51	316.13	978.09	88.14	-0.1014	0.0602	100.51	50.27	536.26	81.94	94.38
3	644.43	367.46	1063.49	97.63	-0.1363	0.0667	-126.37	42.92	557.88	81.66	96.18
4	1305.06	554.54	2150.89	213.25	0.5750	0.2946	654.53	133.71	781.51	98.57	0.87
5	1091.30	767.07	1458.71	85.62	0.2710	0.0978	867.76	93.80	505.43	22.24	0.09
6	919.69	400.20	1532.22	149.12	0.1266	0.1493	-88.25	63.60	851.93	137.71	19.82
7	797.86	420.76	1226.27	105.58	0.0133	0.0919	66.83	12.20	785.78	102.90	47.76
8	770.74	334.98	1226.10	111.46	-0.0341	0.0905	356.51	88.58	480.00	26.99	67.85
9	938.89	217.63	1836.75	190.82	0.1511	0.1934	-180.23	52.88	-178.24	78.69	23.04
10	993.69	327.99	1899.39	196.61	0.1745	0.2071	-696.34	145.81	-20.23	45.50	20.11
11	717.01	506.41	985.32	63.65	-0.0522	0.0491	47.54	19.60	629.91	57.77	85.65
12	733.51	268.14	1213.67	118.67	-0.0381	0.0955	183.39	50.54	348.04	44.15	68.59
13	715.34	363.63	1166.70	107.98	-0.0666	0.0835	-572.36	105.00	414.43	53.43	79.88
14	842.41	172.87	1685.14	194.25	0.0550	0.1799	-712.40	173.04	-157.87	67.12	43.11
15	656.51	311.33	1176.06	116.20	-0.1028	0.0839	470.81	98.33	309.98	52.15	88.60
16	677.25	270.67	1173.45	112.14	-0.0789	0.0822	-110.54	38.95	-594.68	108.17	83.87
17	604.28	462.03	766.28	37.33	0.0046	0.0244	-94.13	8.97	494.02	28.45	44.86
18	652.03	234.67	1216.52	134.68	-0.1117	0.0964	-546.67	119.72	187.59	76.17	87.58
19	640.07	103.05	1574.96	188.81	-0.1008	0.1397	548.46	171.81	292.57	124.32	80.18
20	631.96	92.48	1580.49	179.40	-0.1247	0.1306	-433.94	149.56	379.80	164.03	85.74

Table A.4: Orbit parameters using μ of initial Gaia catalog and Model I

Pal	v_{av}	v_{min}	v_{max}	v_{sdev}	E_{av}	E_{sdev}	U_{av}	U_{sdev}	V_{av}	V_{sdev}	Bound %
1	789.37	419.23	1258.42	114.95	0.1512	0.0974	305.72	61.64	-585.77	100.17	3.84
2	312.54	63.24	819.71	117.00	-0.1126	0.0421	48.39	78.99	258.58	128.56	97.89
3	412.61	113.80	1045.76	102.60	-0.1195	0.0466	-70.47	73.49	371.91	98.85	97.98
4	124.13	67.07	204.68	20.07	-0.1860	0.0020	31.65	16.61	117.46	24.53	100.00
5	1160.72	779.32	1641.62	108.33	0.5000	0.1323	916.11	113.13	513.53	31.96	0.00
6	1233.15	524.41	2181.04	216.12	0.6378	0.2901	-34.07	88.54	1177.69	207.23	0.05
7	782.08	384.22	1390.79	126.20	0.1481	0.1090	69.46	19.27	762.73	122.75	5.43
8	683.91	362.42	1142.89	106.14	0.0442	0.0775	341.52	97.85	448.57	30.56	31.39
9	881.24	251.38	1668.95	189.32	0.2413	0.1829	-152.03	67.08	-171.44	95.06	5.98
10	933.75	314.21	1918.16	198.46	0.2589	0.1978	-641.98	147.16	8.88	70.52	6.21
11	581.68	170.25	1066.07	97.20	0.0041	0.0608	-5.66	36.47	457.89	91.63	51.34
12	525.08	212.91	959.23	101.90	-0.0317	0.0605	112.23	50.39	297.04	73.38	74.28
13	587.57	299.20	1110.58	100.50	-0.0092	0.0651	-448.67	100.74	365.06	70.17	61.21
14	273.51	76.14	580.86	58.71	-0.1496	0.0185	115.70	57.43	209.44	34.56	100.00
15	699.83	299.55	1248.38	127.81	0.0748	0.0982	508.30	107.07	302.24	52.95	23.29
16	424.16	62.53	837.56	102.00	-0.0805	0.0467	41.77	44.56	406.41	101.16	94.05
17	571.64	387.60	825.79	49.59	-0.0149	0.0304	-83.47	12.06	481.06	44.80	70.74
18	553.13	89.86	1227.05	146.78	-0.0271	0.0922	-409.24	135.61	195.17	88.02	68.56
19	768.75	79.51	1872.96	251.77	0.1541	0.2228	682.99	234.47	207.40	162.27	26.63
20	904.94	192.83	2122.11	246.04	0.2541	0.2506	-614.34	199.35	541.13	216.34	12.52

Table A.5: Orbit parameters using μ of initial Gaia catalog and Model II

Pal	v_{av}	v_{min}	v_{max}	v_{sdev}	E_{av}	E_{sdev}	U_{av}	U_{sdev}	V_{av}	V_{sdev}	Bound %
1	791.08	393.30	1290.19	115.12	0.1780	0.0981	306.07	61.41	-588.23	100.35	1.20
2	313.29	64.03	828.38	118.51	-0.0870	0.0429	51.02	79.26	257.57	129.98	95.56
3	410.92	98.94	885.24	104.70	-0.0944	0.0476	-70.54	74.63	369.69	102.26	95.73
4	122.55	66.33	204.42	19.92	-0.1607	0.0020	31.45	16.73	115.86	24.34	100.00
5	1162.22	813.84	1638.56	109.06	0.5277	0.1334	917.76	114.21	511.79	31.59	0.00
6	1231.68	446.88	2184.57	216.81	0.6615	0.2914	-36.79	87.92	1175.24	208.17	0.03
7	782.00	352.93	1351.09	125.16	0.1732	0.1079	69.80	19.19	762.37	121.86	2.19
8	681.99	370.75	1186.81	105.71	0.0685	0.0771	340.27	97.28	446.97	30.66	18.49
9	886.05	296.24	1668.38	191.95	0.2718	0.1863	-153.01	67.33	-175.13	97.54	3.67
10	931.49	266.32	1909.96	201.85	0.2832	0.2018	-642.09	150.33	5.61	70.99	4.06
11	581.66	238.39	1101.61	96.09	0.0293	0.0601	-5.54	36.59	457.20	90.36	34.36
12	523.59	221.97	1010.00	101.51	-0.0072	0.0600	111.74	50.11	295.57	73.78	60.96
13	589.93	274.33	1018.07	103.35	0.0182	0.0673	-452.59	103.09	363.91	70.75	44.81
14	273.19	83.00	564.42	59.83	-0.1240	0.0188	115.98	57.69	208.43	35.50	99.99
15	696.48	329.43	1320.62	126.63	0.0977	0.0969	506.25	106.17	300.90	52.89	14.68
16	421.83	75.78	806.88	101.92	-0.0562	0.0465	42.45	45.04	403.67	101.20	88.33
17	569.32	409.90	789.07	48.83	0.0091	0.0298	-83.35	11.82	478.66	44.26	40.47
18	550.05	168.91	1217.26	145.66	-0.0034	0.0909	-406.36	134.87	193.10	87.80	59.51
19	764.40	62.12	2180.45	251.20	0.1759	0.2216	679.36	233.73	201.02	162.12	21.35
20	901.63	100.04	2063.11	251.25	0.2779	0.2566	-612.00	202.21	539.29	217.87	9.58

Table A.6: Orbit parameters using μ of initial Gaia catalog and Model III

Pal	v_{av}	v_{min}	v_{max}	v_{sdev}	E_{av}	E_{sdev}	U_{av}	U_{sdev}	V_{av}	V_{sdev}	Bound %
1	792.37	420.29	1397.23	115.94	0.0084	0.0992	304.92	61.15	-589.33	100.83	51.07
2	312.27	63.38	769.26	117.72	-0.2577	0.0423	48.94	78.56	257.66	128.99	100.00
3	411.31	103.65	1070.36	104.39	-0.2643	0.0478	-70.13	74.07	370.39	100.49	99.95
4	121.92	66.18	199.33	19.95	-0.3316	0.0020	31.70	16.70	115.05	24.63	100.00
5	1160.25	776.99	1595.51	109.83	0.3547	0.1343	916.16	114.70	511.34	31.54	0.04
6	1231.30	431.79	2164.23	216.84	0.4901	0.2906	-35.55	87.25	1175.33	208.06	1.40
7	777.25	379.23	1361.20	123.37	-0.0016	0.1059	69.43	19.12	757.73	119.92	56.28
8	682.73	369.41	1122.34	106.75	-0.1016	0.0781	341.02	97.73	446.80	30.74	89.60
9	886.82	267.57	1619.61	188.39	0.1009	0.1824	-153.19	67.22	-176.18	95.11	32.01
10	929.06	286.65	1719.71	200.34	0.1103	0.1998	-640.41	148.24	4.21	69.82	32.63
11	579.18	176.39	1031.26	96.65	-0.1429	0.0601	-4.82	36.30	455.87	90.08	98.00
12	520.37	228.88	1020.08	101.71	-0.1799	0.0600	110.53	50.06	294.16	72.58	98.98
13	587.07	301.73	1056.93	101.59	-0.1547	0.0659	-450.55	102.43	361.64	70.63	97.37
14	270.89	83.89	521.62	59.06	-0.2957	0.0182	114.72	56.60	206.99	35.14	100.00
15	699.09	344.45	1248.68	125.02	-0.0715	0.0955	508.79	104.69	300.56	53.02	79.44
16	420.09	70.24	850.36	103.54	-0.2275	0.0469	42.56	45.19	402.10	102.65	99.94
17	569.89	393.41	795.56	48.99	-0.1614	0.0300	-83.45	11.99	479.09	44.70	99.99
18	551.31	140.38	1345.05	146.25	-0.1734	0.0916	-409.34	134.90	191.88	88.10	95.23
19	766.93	75.48	1806.49	252.33	0.0073	0.2224	681.79	236.07	200.69	160.82	57.79
20	898.65	201.01	2029.41	243.58	0.1030	0.2454	-607.55	195.28	541.34	219.63	39.74

Table A.7: Orbit parameters using the in this work obtained μ and Model I ("ne" means non error weighted)

Pal	v_{av}	v_{min}	v_{max}	v_{sdev}	E_{av}	E_{sdev}	U_{av}	U_{sdev}	V_{av}	V_{sdev}	Bound %
2	424.20	81.27	926.23	100.63	-0.071	0.046	204.78	72.83	194.14	113.34	92.12
3	304.55	96.31	684.34	76.10	-0.163	0.026	-149.53	66.92	211.65	79.49	99.99
4	128.08	64.86	204.30	23.17	-0.185	0.003	12.01	13.34	125.41	25.61	100.00
6	146.38	15.66	275.79	38.37	-0.170	0.005	36.22	24.67	135.77	39.66	100.00
9	254.70	134.09	482.26	41.95	-0.149	0.013	-43.82	34.19	219.95	41.29	100.00
12	483.70	263.18	803.13	69.98	-0.056	0.039	62.87	31.17	338.01	42.42	91.63
13	187.36	53.66	339.70	36.01	-0.176	0.007	-29.95	36.93	179.76	38.78	100.00
14	201.92	70.22	429.20	50.80	-0.168	0.012	34.32	57.92	173.93	45.23	100.00
15	241.25	176.25	317.97	18.18	-0.159	0.005	-66.01	22.18	229.98	21.15	100.00
16	294.28	57.07	651.08	75.30	-0.132	0.024	38.28	31.27	279.10	76.68	99.97
17	348.05	237.46	480.40	30.49	-0.123	0.011	-40.32	7.65	312.78	29.11	100.00
18	537.57	176.33	1130.19	123.16	-0.039	0.074	-480.76	119.44	119.92	55.50	74.45
19	151.65	56.16	374.21	42.71	-0.175	0.009	95.90	48.29	103.01	27.77	100.00
20	257.21	80.52	540.84	69.10	-0.169	0.020	-87.87	58.93	214.52	81.19	100.00
2 ne	468.19	70.40	1196.35	155.43	-0.043	0.081	248.61	104.70	132.67	165.34	75.28
3 ne	304.94	107.43	656.45	74.86	-0.163	0.025	-129.17	35.03	243.38	59.88	99.99
4 ne	110.32	64.72	190.59	19.72	-0.188	0.002	24.80	13.33	104.80	24.70	100.00
6 ne	119.61	11.74	242.02	38.56	-0.174	0.005	51.68	25.50	98.01	44.28	100.00
9 ne	239.85	213.28	283.67	8.95	-0.153	0.004	-22.45	9.12	231.23	11.99	100.00
12 ne	491.23	260.60	878.54	83.73	-0.052	0.047	64.69	32.16	341.24	50.63	86.49
13 ne	190.64	70.74	432.16	44.53	-0.175	0.010	19.14	59.01	174.63	56.01	100.00
14 ne	261.49	104.29	527.14	50.71	-0.153	0.015	15.07	50.28	227.38	40.96	100.00
15 ne	226.59	185.42	266.44	10.13	-0.163	0.002	-75.61	13.69	212.75	13.95	100.00
16 ne	279.50	192.04	394.54	27.34	-0.139	0.008	32.60	19.15	272.77	24.11	100.00
17 ne	340.51	279.46	417.97	17.70	-0.126	0.007	-27.90	5.74	324.98	17.98	100.00
18 ne	508.38	151.48	984.38	114.67	-0.056	0.065	-461.27	111.80	104.83	49.08	82.68
19 ne	184.85	54.04	652.04	83.71	-0.167	0.022	92.79	122.39	107.86	38.83	99.93
20 ne	408.20	82.54	1083.62	137.29	-0.109	0.066	-263.42	115.45	267.83	135.93	93.54

Table A.8: Orbit parameters using the in this work obtained μ and Model II ("ne" means non error weighted)

Pal	v_{av}	v_{min}	v_{max}	v_{sdev}	E_{av}	E_{sdev}	U_{av}	U_{sdev}	V_{av}	V_{sdev}	Bound %
2	423.98	85.85	877.85	101.66	-0.046	0.047	203.15	73.09	195.51	114.69	84.29
3	303.19	91.21	713.67	76.20	-0.137	0.026	-149.69	66.09	210.43	78.50	99.88
4	126.51	62.77	203.36	23.02	-0.160	0.003	11.71	13.16	123.87	25.42	100.00
6	145.09	15.21	297.28	38.00	-0.145	0.005	35.88	24.81	134.21	39.73	100.00
9	254.20	138.32	454.72	43.20	-0.123	0.013	-44.87	34.97	218.87	41.49	100.00
12	482.14	275.22	768.92	70.33	-0.032	0.039	62.47	30.76	336.38	43.41	81.37
13	185.99	45.23	329.85	36.73	-0.151	0.007	-29.48	36.18	178.56	39.50	100.00
14	200.62	70.17	459.19	50.71	-0.143	0.012	33.30	57.85	172.70	45.04	100.00
15	239.58	175.43	337.65	18.55	-0.134	0.005	-66.01	22.22	228.20	21.39	100.00
16	293.85	57.17	599.53	74.52	-0.107	0.024	39.08	31.33	277.98	76.14	99.96
17	346.59	231.56	484.43	30.83	-0.098	0.012	-40.24	7.65	311.34	29.59	100.00
18	535.08	167.50	1185.15	122.92	-0.015	0.074	-478.58	119.19	117.29	55.71	64.17
19	149.83	50.69	359.22	42.18	-0.150	0.009	95.21	47.77	100.94	27.89	100.00
20	256.09	81.09	567.96	69.71	-0.143	0.020	-87.87	59.29	212.86	82.19	100.00
2 ne	465.76	70.53	1061.28	153.78	-0.020	0.080	249.15	103.38	126.30	166.52	66.12
3 ne	304.05	98.50	655.18	74.80	-0.137	0.025	-128.90	34.86	242.31	60.15	99.99
4 ne	109.09	64.40	189.06	19.69	-0.162	0.002	24.39	12.99	103.68	24.50	100.00
6 ne	118.14	12.86	243.55	38.33	-0.148	0.005	51.90	25.72	95.96	44.11	100.00
9 ne	238.36	208.58	287.65	8.99	-0.128	0.004	-22.65	9.15	229.72	11.98	100.00
12 ne	491.26	256.79	1083.74	85.13	-0.026	0.048	64.42	32.61	340.65	51.55	74.82
13 ne	189.70	55.57	424.41	43.67	-0.150	0.009	18.75	58.50	173.87	55.29	100.00
14 ne	259.83	85.14	491.00	50.35	-0.128	0.015	14.17	50.23	225.68	40.38	100.00
15 ne	225.04	183.42	260.33	10.04	-0.138	0.002	-75.49	13.69	211.15	13.89	100.00
16 ne	278.45	188.05	398.26	27.32	-0.114	0.008	32.89	19.14	271.65	24.07	100.00
17 ne	338.98	271.82	414.39	17.51	-0.101	0.007	-27.89	5.78	323.36	17.81	100.00
18 ne	507.50	177.19	993.41	115.66	-0.031	0.066	-460.34	113.08	103.37	48.98	72.86
19 ne	182.76	50.69	690.00	82.94	-0.142	0.022	92.24	120.73	106.58	39.23	99.80
20 ne	406.27	81.94	1041.65	136.74	-0.084	0.064	-264.12	114.78	264.28	135.67	89.86

Table A.9: Orbit parameters using the in this work obtained μ and Model III ("ne" means non error weighted)

Pal	v_{av}	v_{min}	v_{max}	v_{sdev}	E_{av}	E_{sdev}	U_{av}	U_{sdev}	V_{av}	V_{sdev}	Bound %
2	424.77	70.53	900.60	102.18	-0.216	0.047	204.96	74.13	192.26	114.93	99.90
3	304.15	95.32	678.64	77.67	-0.307	0.026	-150.85	67.10	209.52	80.39	100.00
4	125.54	65.00	205.75	23.26	-0.331	0.003	11.91	13.35	122.82	25.69	100.00
6	145.00	15.65	290.28	38.17	-0.316	0.005	36.37	24.91	134.01	40.05	100.00
9	253.94	133.51	445.74	43.26	-0.294	0.013	-45.21	34.78	217.35	41.61	100.00
12	481.91	287.78	808.91	69.91	-0.203	0.038	62.72	30.85	335.50	42.77	99.98
13	185.60	50.25	310.62	35.94	-0.322	0.007	-29.81	36.63	178.03	38.68	100.00
14	199.76	70.23	435.66	50.91	-0.314	0.012	33.67	57.91	171.68	45.10	100.00
15	238.94	175.00	332.38	18.24	-0.305	0.005	-65.64	22.17	227.65	21.24	100.00
16	291.32	51.33	653.20	75.21	-0.278	0.024	38.38	31.51	275.64	76.67	100.00
17	345.99	234.84	489.39	30.76	-0.269	0.011	-40.39	7.70	310.35	29.28	100.00
18	536.54	164.76	1094.23	124.27	-0.185	0.075	-480.60	121.14	116.54	55.37	97.77
19	150.31	51.31	385.95	42.74	-0.321	0.009	96.31	48.31	100.53	27.73	100.00
20	254.30	79.37	618.48	68.30	-0.314	0.019	-87.67	58.86	211.47	79.79	100.00
2 ne	467.29	67.63	1163.97	153.64	-0.189	0.080	248.50	103.52	130.69	163.80	97.12
3 ne	303.22	99.53	632.44	74.79	-0.307	0.025	-129.52	34.99	240.99	59.92	100.00
4 ne	108.47	64.21	188.80	19.74	-0.333	0.002	24.12	13.05	103.09	24.53	100.00
6 ne	117.46	12.91	254.38	38.39	-0.319	0.004	51.67	25.41	95.47	44.24	100.00
9 ne	237.79	206.21	286.44	8.96	-0.299	0.004	-23.01	9.19	229.04	11.96	100.00
12 ne	491.56	208.54	874.28	84.35	-0.197	0.047	64.73	31.85	340.25	51.11	99.82
13 ne	188.31	55.13	475.16	44.91	-0.321	0.010	19.21	59.12	171.93	56.55	100.00
14 ne	260.18	107.15	513.56	50.49	-0.299	0.015	14.43	50.53	225.69	40.64	100.00
15 ne	224.34	186.64	262.95	10.14	-0.309	0.002	-75.25	13.72	210.48	14.11	100.00
16 ne	277.58	184.52	404.91	27.13	-0.285	0.008	32.82	19.13	270.81	23.82	100.00
17 ne	338.14	277.20	414.56	17.58	-0.273	0.007	-27.98	5.79	322.39	17.89	100.00
18 ne	506.63	164.04	1056.20	114.00	-0.203	0.065	-459.96	111.61	101.76	47.96	99.08
19 ne	182.64	49.38	703.87	82.76	-0.313	0.022	93.45	119.92	106.54	39.00	100.00
20 ne	404.91	82.28	1145.65	138.54	-0.255	0.066	-262.79	116.89	262.41	137.08	99.29

Appendix B

Radial velocity fits of interesting stars

Now the radial velocity fits for the interesting candidates (Pal02, Pal12, Pal18) are presented. The average spectrum of the star is plotted in red. Prominent lines are centred and noted at the right in \AA . In the fit (blue) of the spectrum, the prominent lines and a range of $\pm 40\text{\AA}$ around them was fitted. Following fits were obtained by using the stellar parameters of SSPP and only fitting v_{rad} . The value in square brackets denotes the radial velocity from SSPP. (see Sect. 4.1.2)

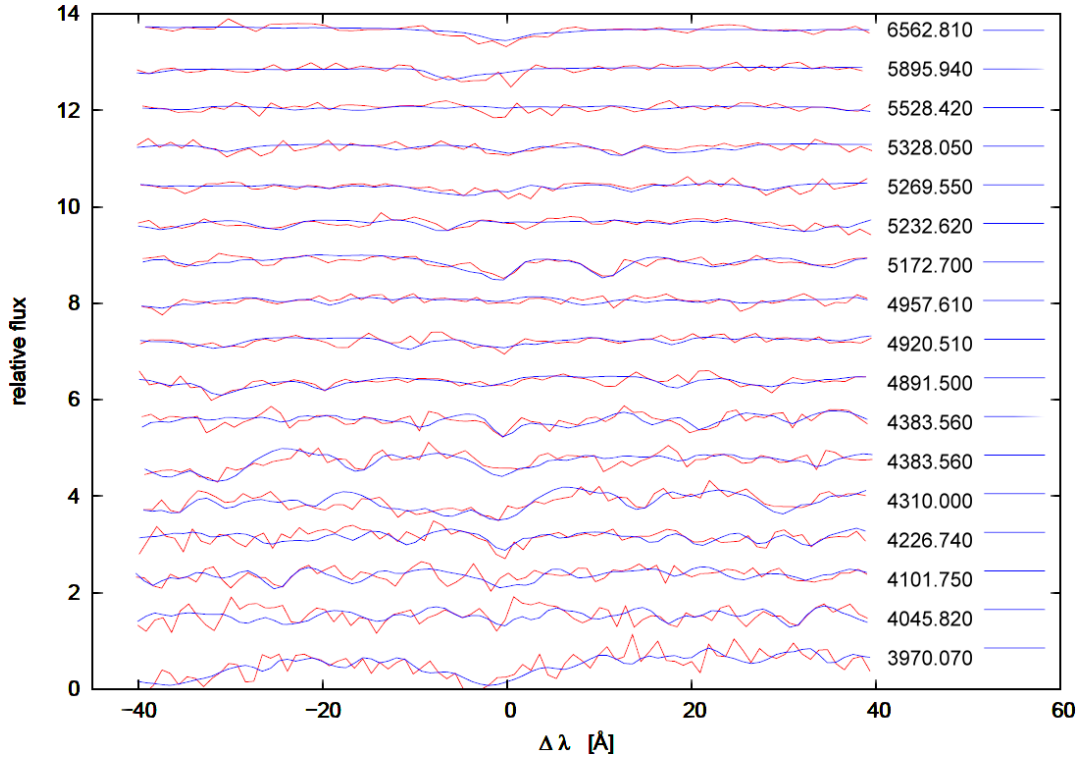


Figure B.1: Radial velocity fit Pal02: $v_{\text{rad}} = (-30.95 \pm 0.73) [-25.60] \text{ km s}^{-1}$

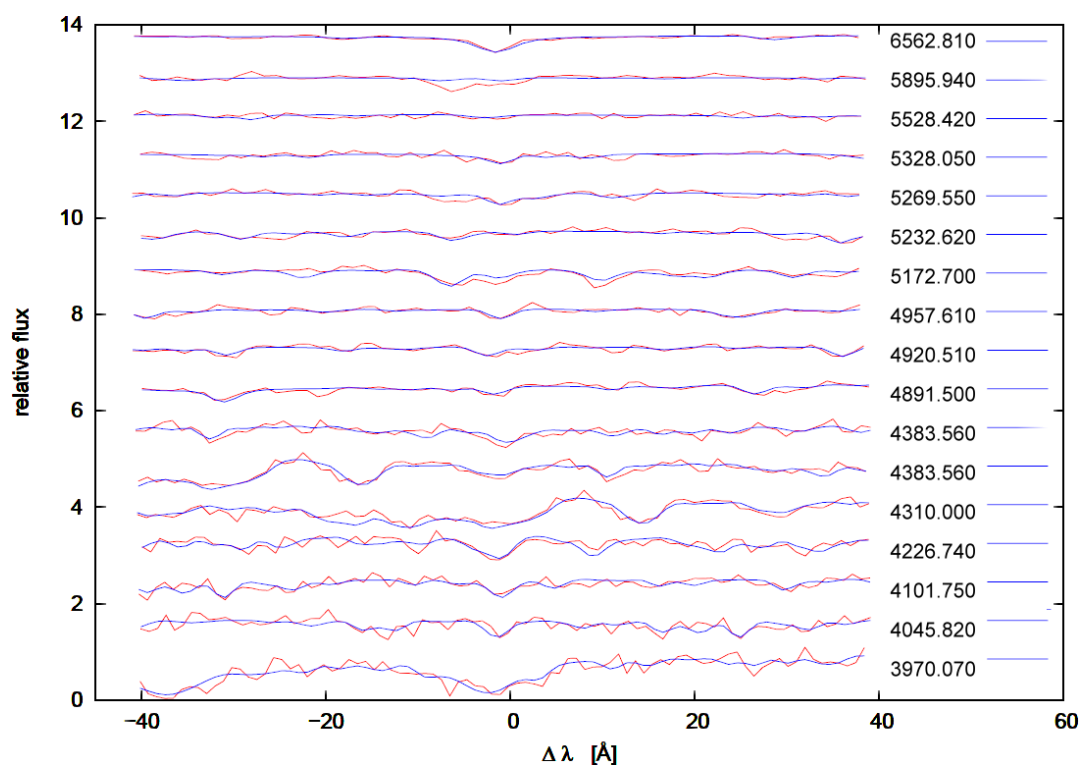


Figure B.2: Radial velocity fit Pal12: $v_{\text{rad}} = (-67.12 \pm 0.96) [-62.40] \text{ km s}^{-1}$

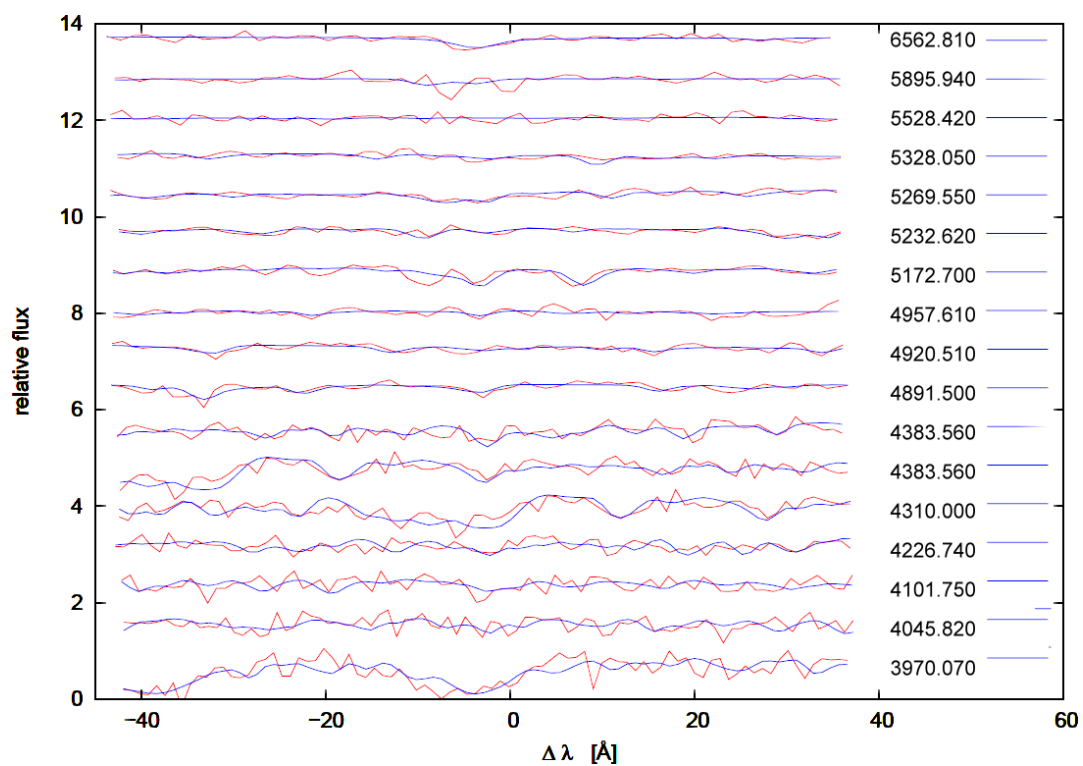


Figure B.3: Radial velocity fit Pal18: $v_{\text{rad}} = (-173.87 \pm 0.83) [-205.10] \text{ km s}^{-1}$

Appendix C

Proper motion fits of all stars

In the following the error weighted proper motion-fits of all 14 analysed candidates are presented, except Pal15 which is presented in Sect. 4.2.3.

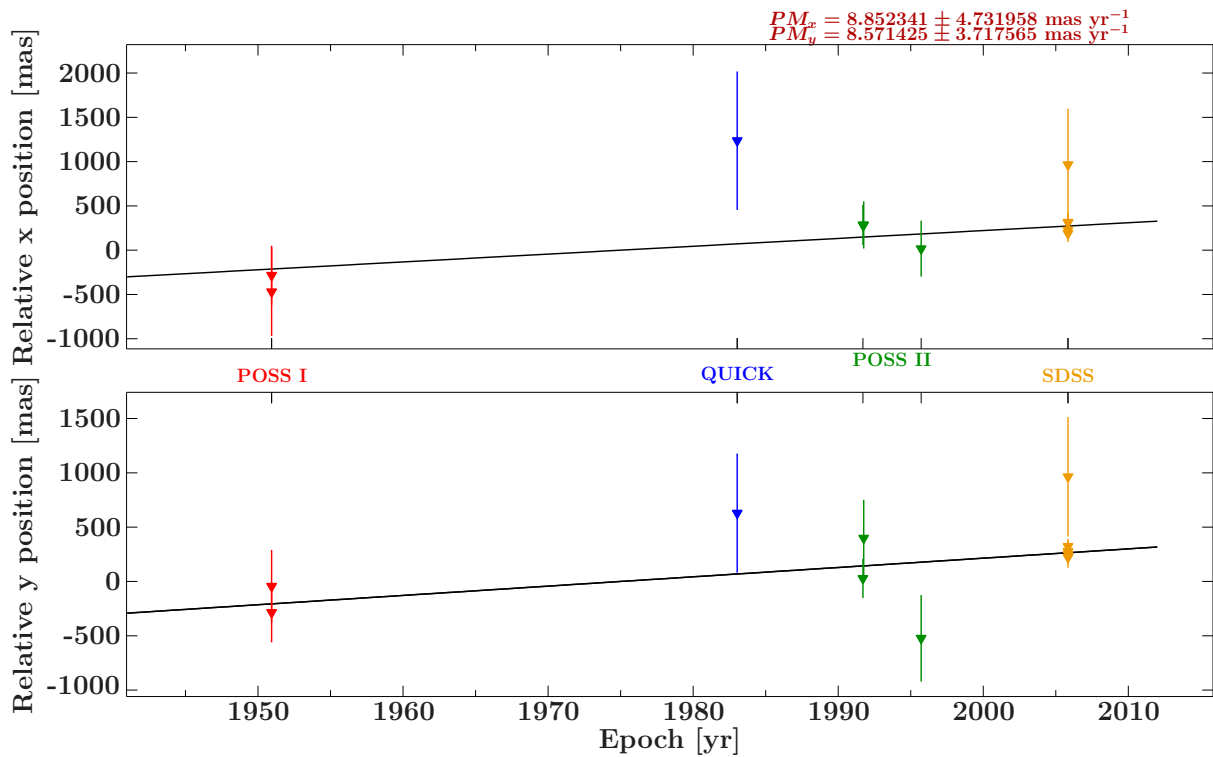


Figure C.1: Proper motion Measurement Pal02

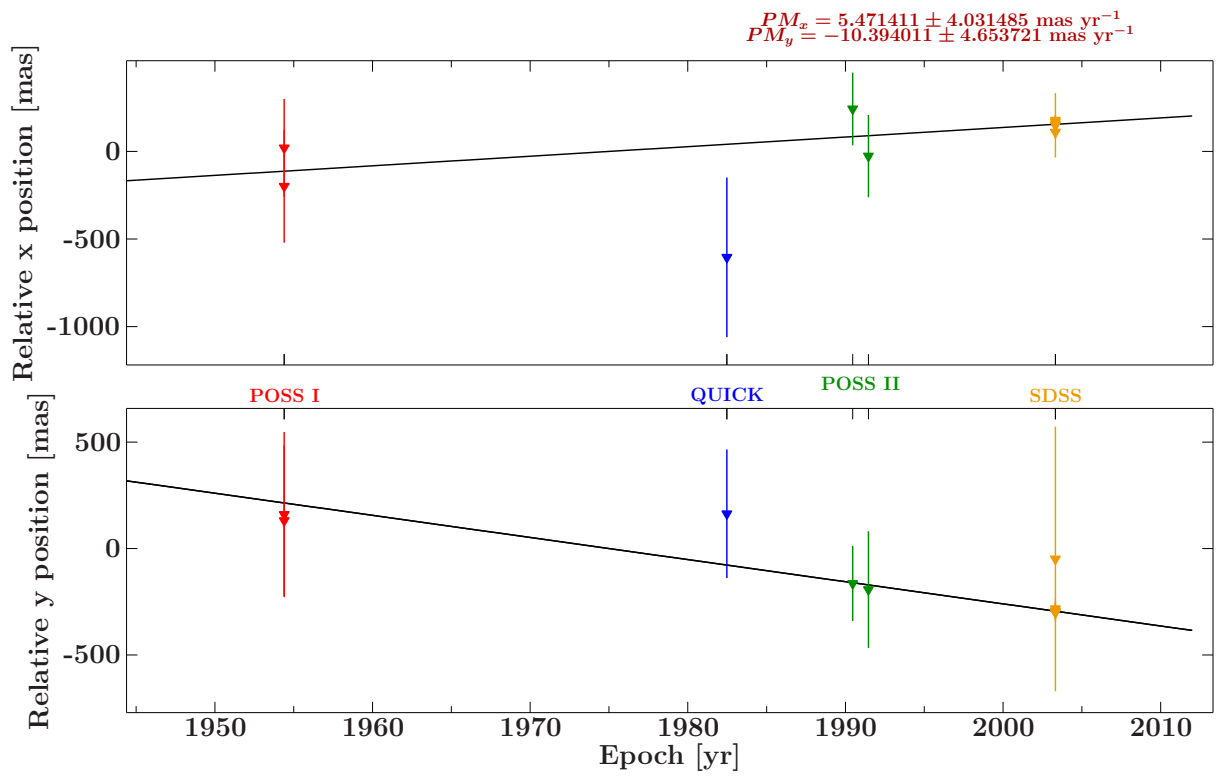


Figure C.2: Proper motion Measurement Pal03

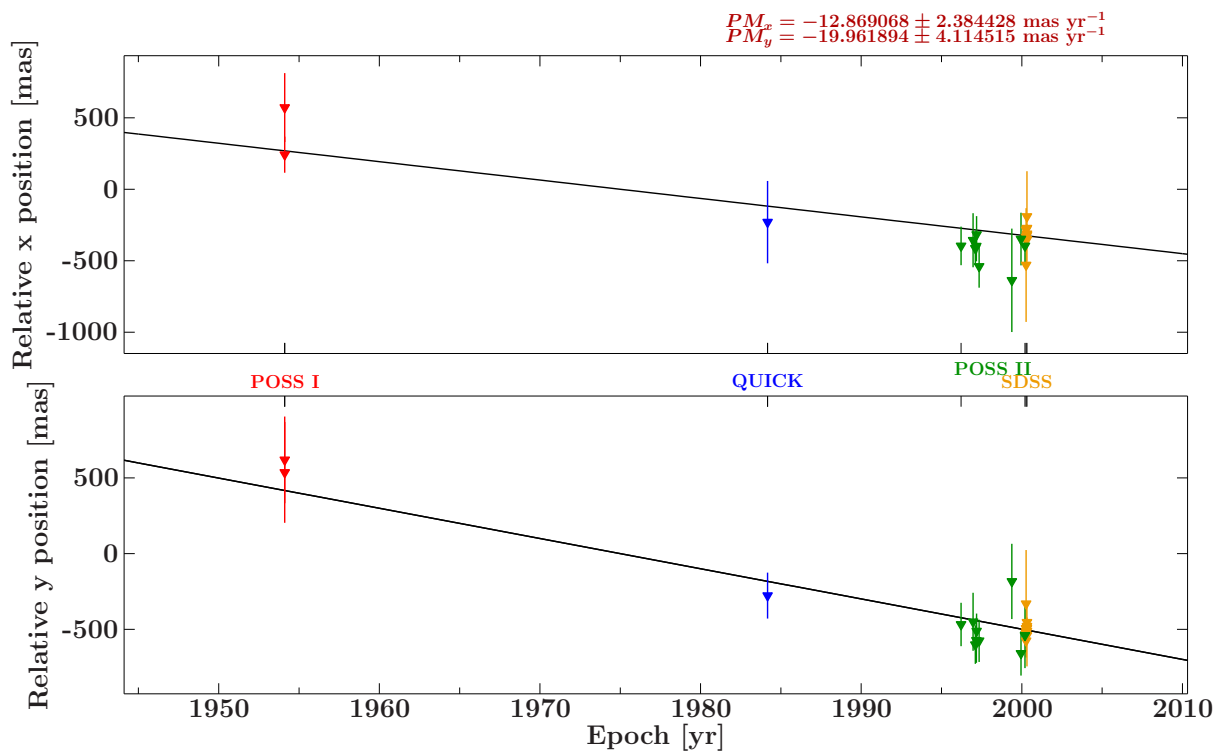


Figure C.3: Proper motion Measurement Pal04

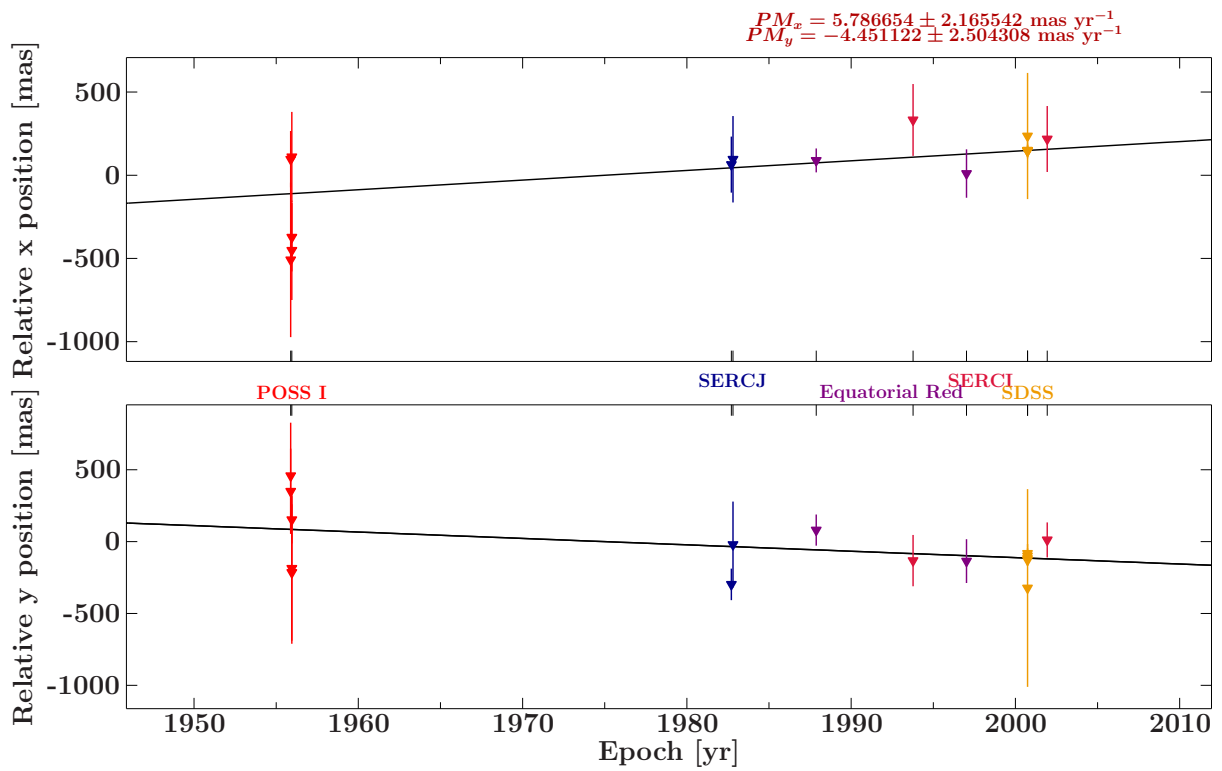


Figure C.4: Proper motion Measurement Pal06

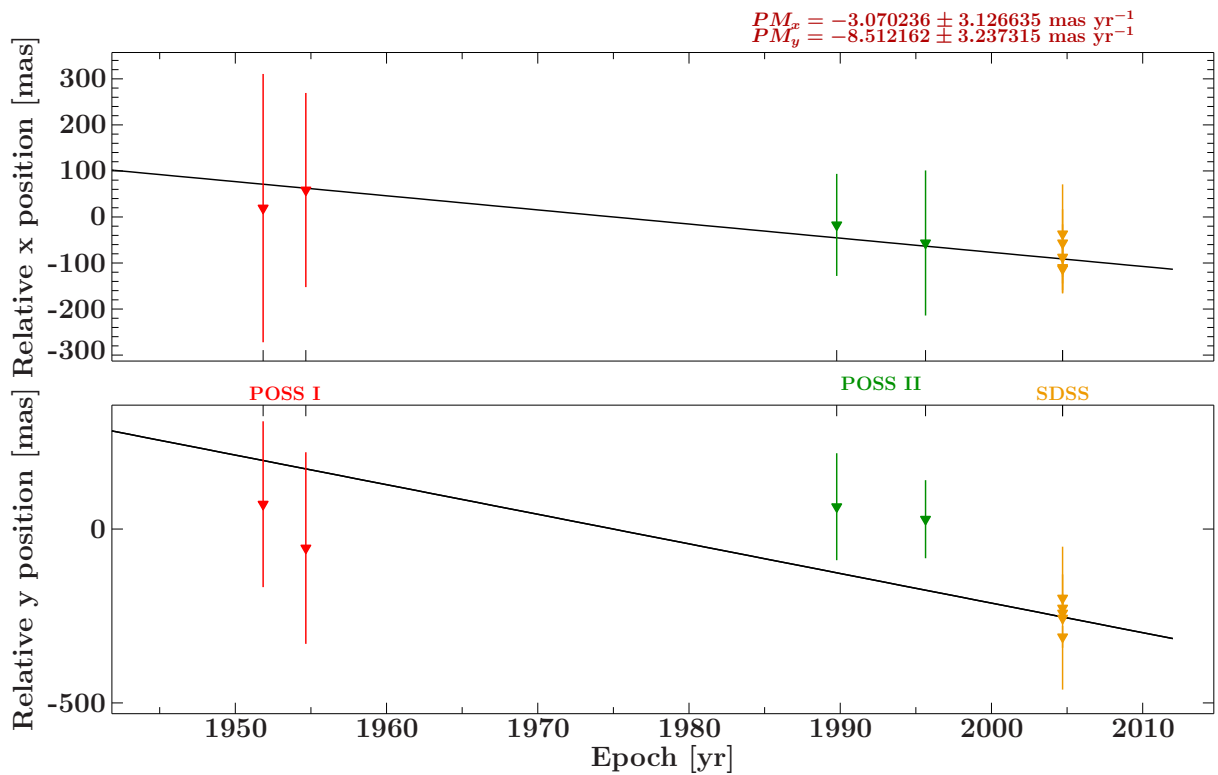


Figure C.5: Proper motion Measurement Pal09

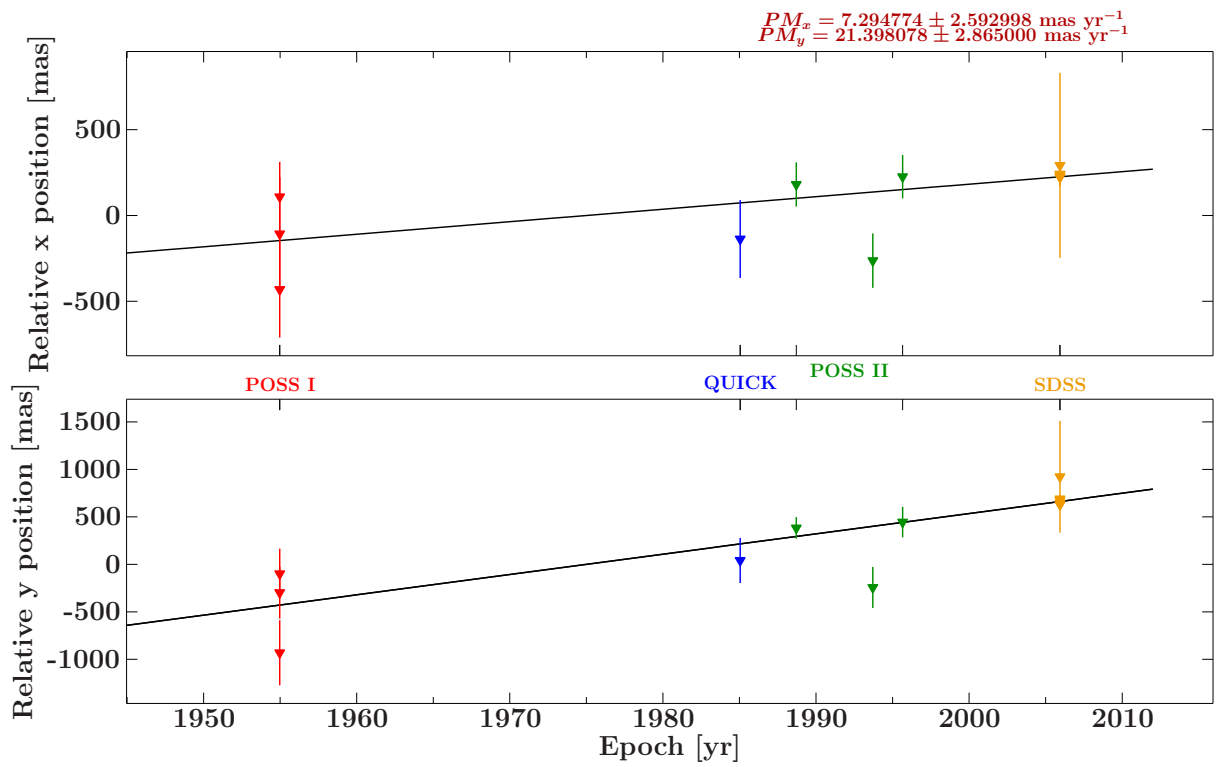


Figure C.6: Proper motion Measurement Pal12

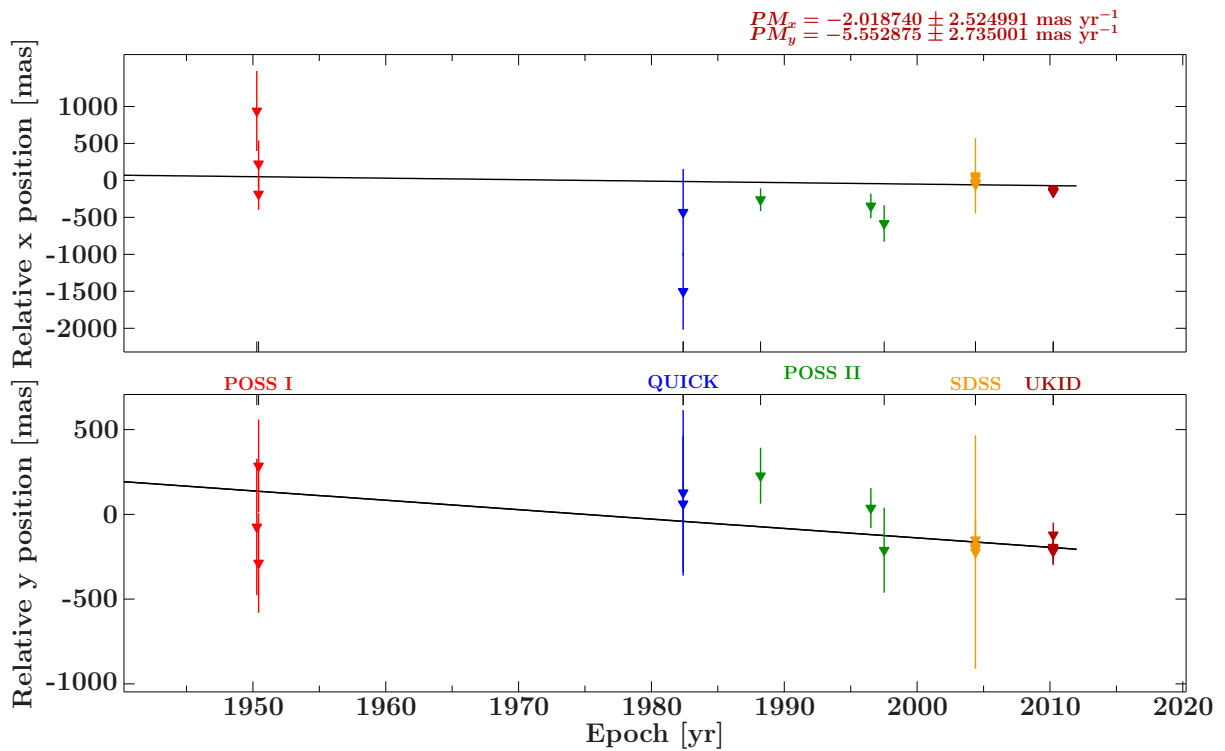


Figure C.7: Proper motion Measurement Pal13

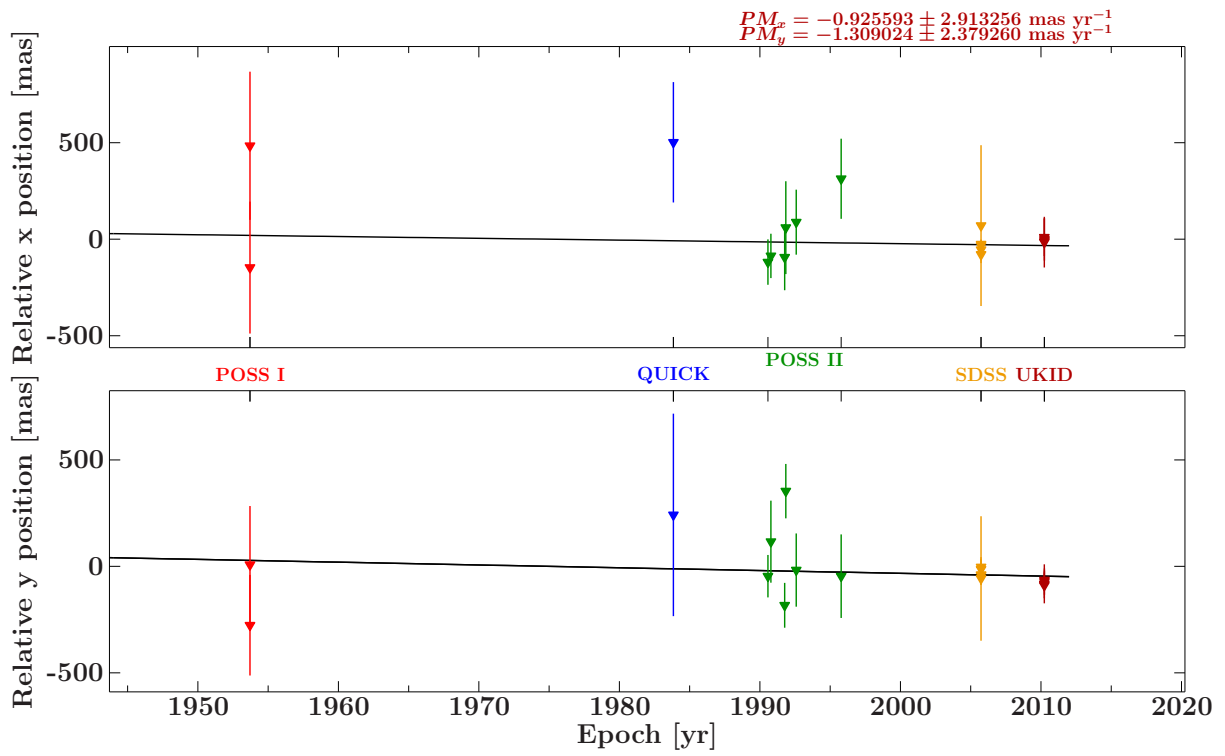


Figure C.8: Proper motion Measurement Pal14

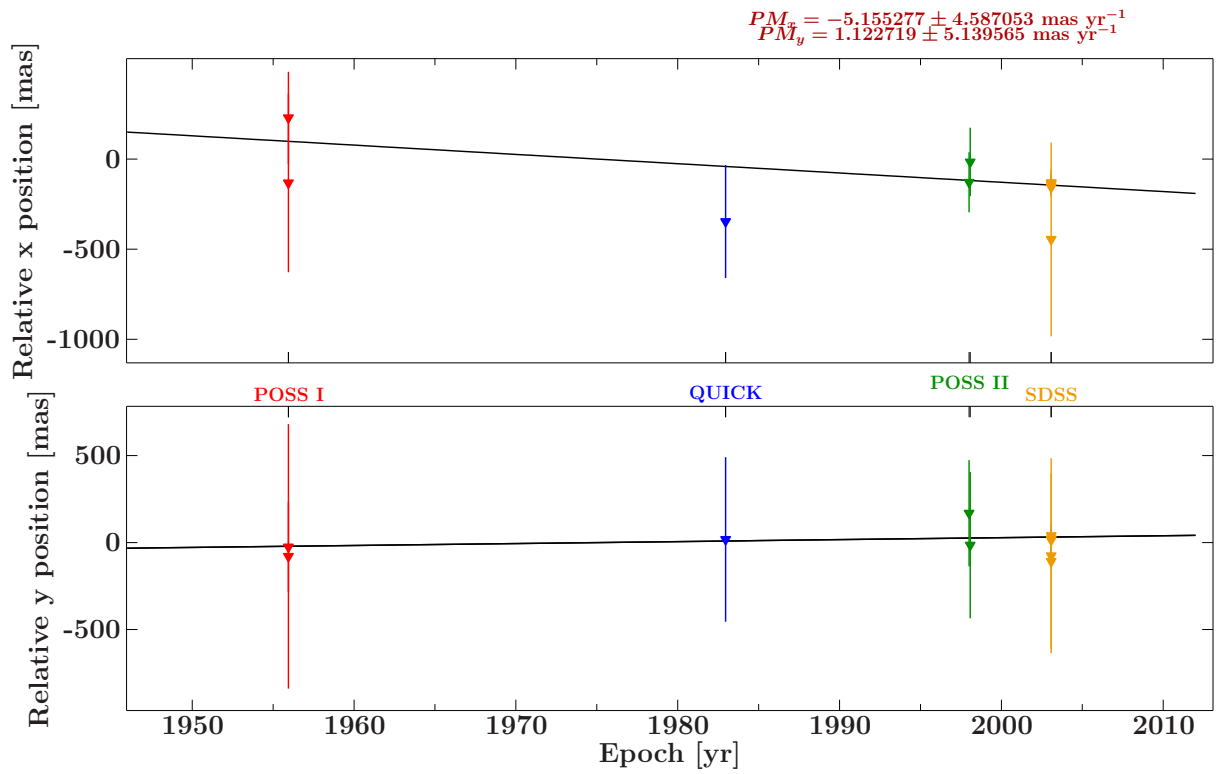


Figure C.9: Proper motion Measurement Pal16

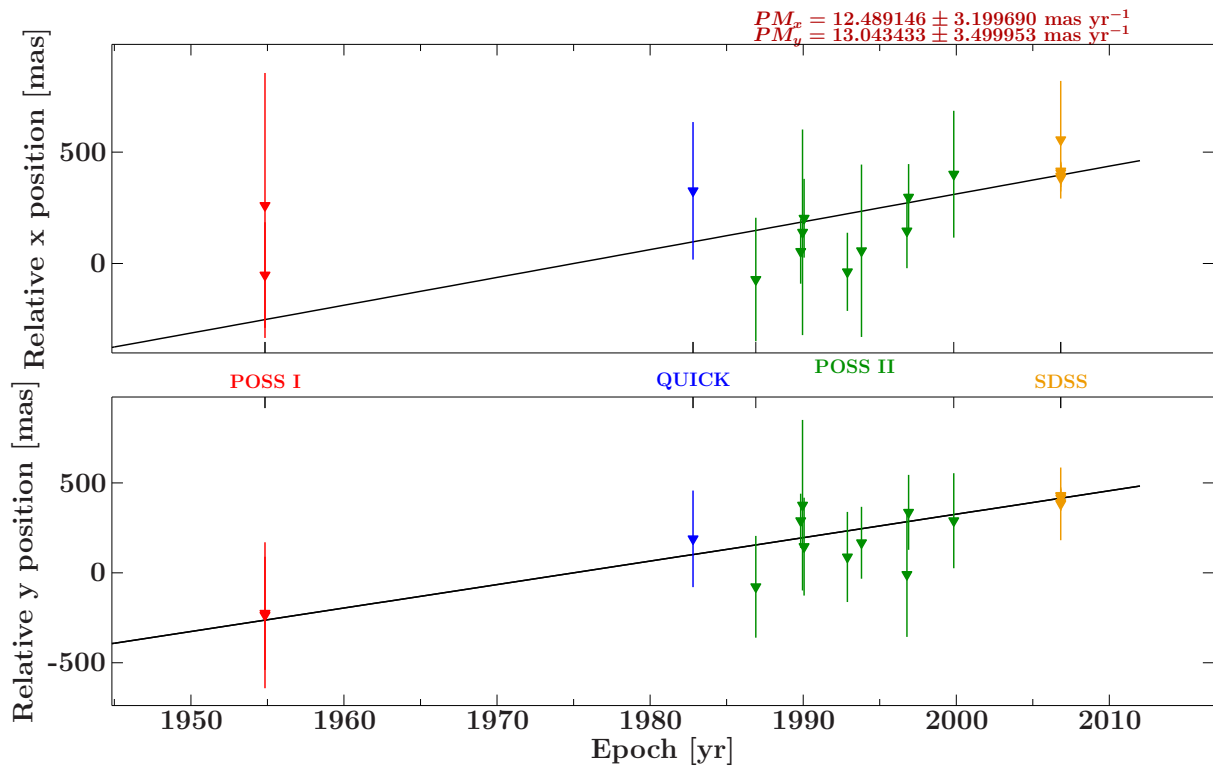


Figure C.10: Proper motion Measurement Pal17

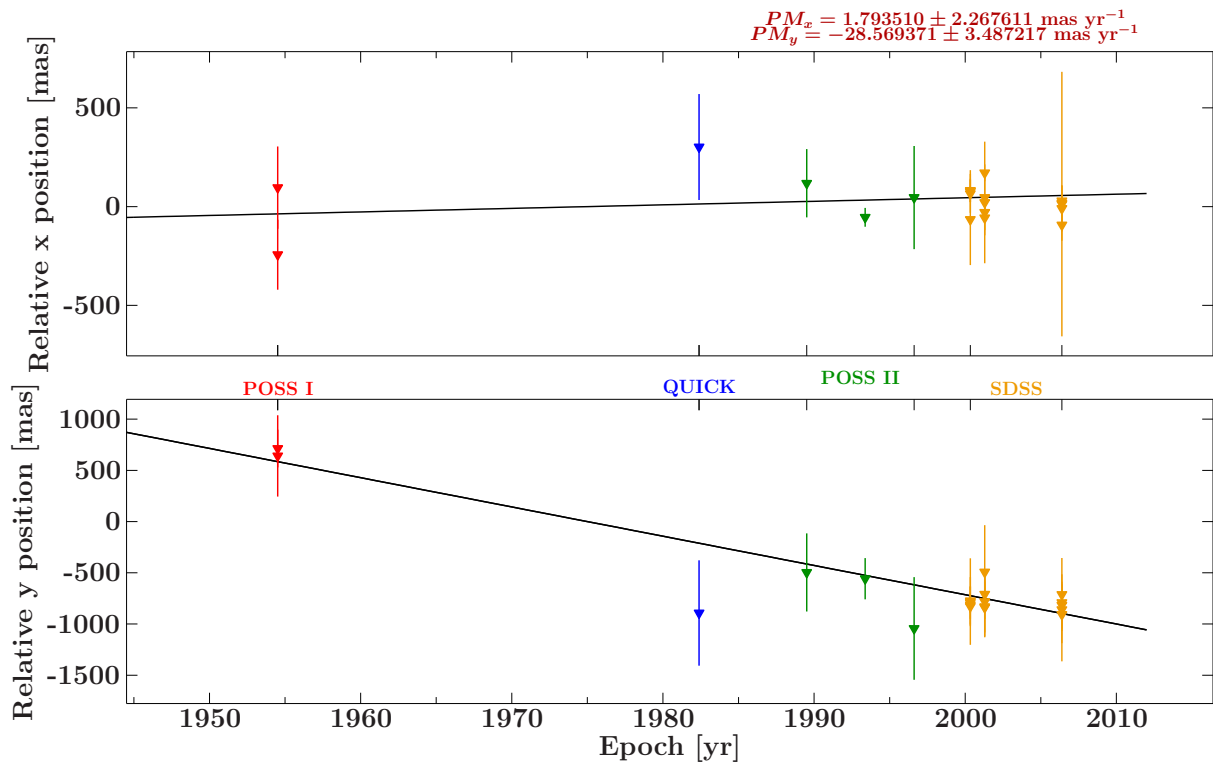


Figure C.11: Proper motion Measurement Pal18

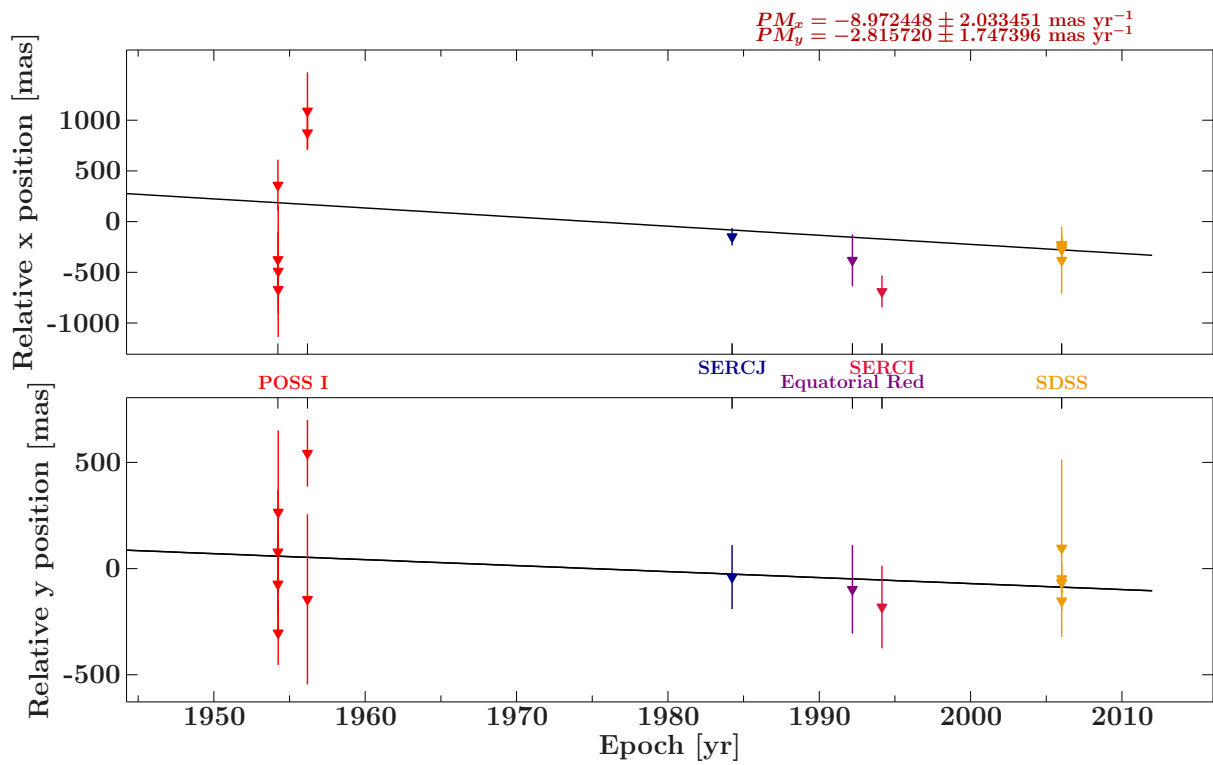


Figure C.12: Proper motion Measurement Pal19

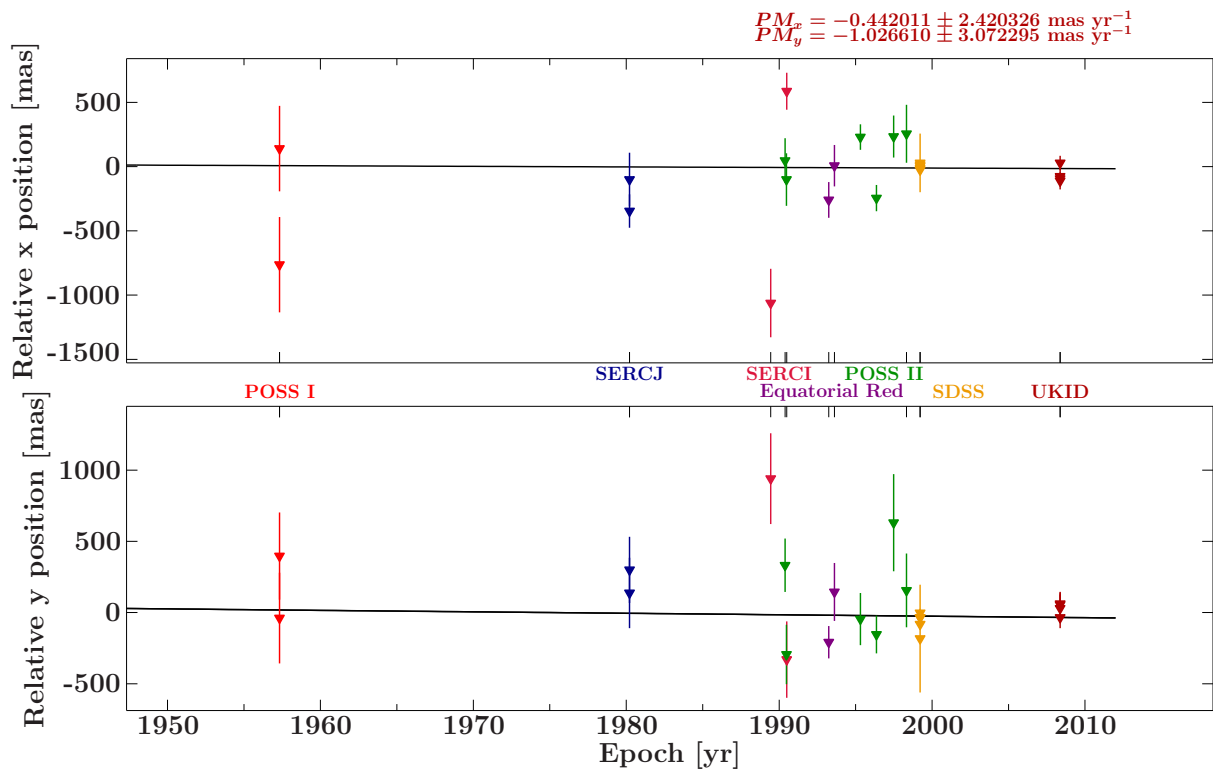


Figure C.13: Proper motion Measurement Pal20

List of Figures

1.1	HRD	2
1.2	Structure of the Milky Way	3
1.3	Velocity components	4
3.1	ratio of transversal to radial velocity	12
3.2	Doubts on Palladino et al. (2014) by theoretical model	14
4.1	Radial velocity fit Pal04	18
4.2	Propermotion Measurement Pal15	21
4.3	Ratio of transverse to radial velocity	22
5.1	Pal02: Velocity Histogram	24
5.2	Pal02: possible Origins - Galactic disk passages within 100kpc	25
5.3	Pal02: possible Origins - Galactic disk passages within 30kpc	25
5.4	Pal02: Orbit 2D-projection	26
5.5	Pal12: Velocity Histogram	26
5.6	Pal12: possible Origins - Galactic disk passages within 100kpc	27
5.7	Pal12: Orbit 3D	27
5.8	Pal12: Orbit 2D-projection	27
5.9	Pal18: Velocity Histogram	28
5.10	Pal18: possible Origins - Galactic disk passages within 100kpc	28
5.11	Pal18: possible Origins projection on disk - without a Galactic disk passage within 100kpc	28
5.12	Pal18: Orbit 2D-projection	29
5.13	Pal18: Orbit 3D	29
5.14	Pal18: Orbit 3D Zoom	29
5.15	Pal02: Orbit 3D	30
5.16	U-V-Diagram	31
5.17	examined stars in comparison to the sample of Sakamoto et al. (2003)	31
B.1	Radial velocity fit Pal02	43
B.2	Radial velocity fit Pal12	44
B.3	Radial velocity fit Pal18	44
C.1	Proper motion Measurement Pal02	45
C.2	Proper motion Measurement Pal03	46
C.3	Proper motion Measurement Pal04	46
C.4	Proper motion Measurement Pal06	47
C.5	Proper motion Measurement Pal09	47
C.6	Proper motion Measurement Pal12	48
C.7	Proper motion Measurement Pal13	48
C.8	Proper motion Measurement Pal14	49
C.9	Proper motion Measurement Pal16	49
C.10	Proper motion Measurement Pal17	50

C.11 Proper motion Measurement Pal18	50
C.12 Proper motion Measurement Pal19	51
C.13 Proper motion Measurement Pal20	51

List of Tables

2.1	Parameters obtained by Irrgang et al. (2013) for different potential models	9
3.1	Stars of Palladino	12
3.2	Comparison of proper motion components between different catalogs	16
4.1	proper motions obtained in this work in comparison to SDSS	22
5.1	bound-probabilities	23
A.1	Orbit parameters using SDSS obtained μ and Model I	35
A.2	Orbit parameters using SDSS obtained μ and Model II	36
A.3	Orbit parameters using SDSS obtained μ and Model III	36
A.4	Orbit parameters using μ of initial Gaia catalog and Model I	37
A.5	Orbit parameters using μ of initial Gaia catalog and Model II	37
A.6	Orbit parameters using μ of initial Gaia catalog and Model III	38
A.7	Orbit parameters using the in this work obtained μ and Model I	39
A.8	Orbit parameters using the in this work obtained μ and Model II	40
A.9	Orbit parameters using the in this work obtained μ and Model III	41

Bibliography

- Allen C., Santillan A., 1991, *Rev. Mexicana Astron. Astrofis.*22, 255
- Brown W.R., Geller M.J., Kenyon S.J., 2014, ArXiv e-prints
- Brown W.R., Geller M.J., Kenyon S.J., Kurtz M.J., 2005, *ApJ* 622, L33
- Edelmann H., Napiwotzki R., Heber U., et al., 2005, *ApJ* 634, L181
- Genzel R., Schödel R., Ott T., et al., 2003, *ApJ*594, 812
- Heber U., Edelmann H., Napiwotzki R., et al., 2008, *A&A* 483, L21
- Hernquist L., 1990, *ApJ* 356, 359
- Hills J.G., 1988, *Nat* 331, 687
- Hirsch H.A., Heber U., O'Toole S.J., Bresolin F., 2005, *A&A* 444, L61
- Irrgang A., Wilcox B., Tucker E., Schiefelbein L., 2013 549, A137
- Kenyon S.J., Bromley B.C., Brown W.R., Geller M.J., 2014, ArXiv e-prints
- Li Y., Luo A., Zhao G., et al., 2012, *Astrophys. J., Lett.* 744, L24
- Łokas E.L., Mamon G.A., 2001, *MNRAS*321, 155
- Miyamoto M., Nagai R., 1975, *PASJ*27, 533
- Monet D.G., Levine S.E., Canzian B., et al., 2003, *AJ* 125, 984
- Munari U., Sordo R., Castelli F., Zwitter T., 2005, *A&A* 442, 1127
- Munn J.A., Monet D.G., Levine S.E., et al., 2004, *ApJ* 127, 3034
- Napiwotzki R., Yungelson L., Nelemans G., et al., 2004, In: R. W. Hilditch, H. Hensberge, & K. Pavlovski (ed.) *Spectroscopically and Spatially Resolving the Components of the Close Binary Stars*, Vol. 318. *Astronomical Society of the Pacific Conference Series*, p.402
- Navarro J.F., Frenk C.S., White S.D.M., 1997, *ApJ* 490, 493
- Palladino L.E., Schlesinger K.J., Holley-Bockelmann K., et al., 2014, *ApJ* 780, 7
- Pauli E.M., Napiwotzki R., Heber U., et al., 2006, *A&A* 447, 173
- Roeser S., Demleitner M., Schilbach E., 2010, *AJ* 139, 2440
- Sakamoto T., Chiba M., Beers T.C., 2003, *A&A* 397, 899
- Schödel R., Ott T., Genzel R., et al., 2003, *ApJ* 596, 1015
- Schönrich R., Binney J., Dehnen W., 2010, *MNRAS* 403, 1829

- Sherwin B.D., Loeb A., O'Leary R.M., 2008, MNRAS 386, 1179
- Smart R.L., Nicastro L., 2014, VizieR Online Data Catalog 1324, 0
- Voigt H.H., 2012, Abriss der Astronomie, WILEY-VCH
- Wilkinson M.I., Evans N.W., 1999, MNRAS 310, 645
- Yu Q., Tremaine S., 2003, ApJ 599, 1129
- Zacharias N., Finch C.T., Girard T.M., et al., 2012, VizieR Online Data Catalog 1322, 0
- Zacharias N., Monet D.G., Levine S.E., et al., 2004, In: American Astronomical Society Meeting Abstracts, Vol. 36. Bulletin of the American Astronomical Society, p. 1418
- Zhong J., Chen L., Liu C., et al., 2014, Astrophys. J., Lett. 789, L2

Acknowledgements

In the end I want to thank some important people without whom this work wouldn't have been possible.

First my great thanks go to Prof. Dr. Ulrich Heber, who supervised my work in a very kind way. Then special thanks go to Dipl. Phys. Eva Ziegerer, who introduced me into all the methods I used and kindly replied to every question which arose during this work. I even want to thank Dr. Andreas Irrgang for providing the "orbit calculator" programme used in this bachelor thesis. Furthermore I give thanks to all the people in the observatory for providing a warm and relaxed atmosphere at the workplace.

Finally I give my thanks to my parents Claudia and Manfred Volkert, who supported me in all possible ways that are open for non-physicists.

Erklärung

Hiermit erkläre ich, diese Bachelorarbeit in Eigenarbeit angefertigt zu haben, sofern nicht explizit in Text oder Referenzen vermerkt. Diese Arbeit ist der Universität Erlangen-Nürnberg als Voraussetzung für den Erhalt des Abschlusses Bachelor of Science vorgelegt worden. Ich erkläre, dass diese Arbeit weder partiell noch als Ganzes für den Erhalt eines anderweitigen Abschlusses verwendet wurde und wird.

Erlangen 17.09.2014

Ort, Datum

Marco Volkert